Neurobiology of Disease

Implications of Oligomeric Amyloid-Beta (oAβ_{42}) Signaling through $\alpha7\beta2$-Nicotinic Acetylcholine Receptors (nAChRs) on Basal Forebrain Cholinergic Neuronal Intrinsic Excitability and Cognitive Decline

Andrew A. George,[1] Jaime M. Vieira,[2] Cameron Xavier-Jackson,[3] Michael T. Gee,[4] John R. Cirrito,[5] Heather A. Bimonte-Nelson,[2] Marina R. Picciotto,[6] Ronald J. Lukas,[1] and Paul Whiteaker[1]

[1]Department of Neurobiology, Barrow Neurological Institute, St. Joseph's Hospital and Medical Center, Phoenix, Arizona 85013, [2]Department of Psychology, Arizona State University, Tempe, Arizona 87110, [3]Department of Pharmacology, University of Bath, Bath, BA2 7AY, United Kingdom, [4]Department of Physiology, Banner-University Medical Center, University of Arizona, Tucson, Arizona 85724, [5]Division of Biology and Biomedical Sciences, Washington University, St. Louis, Missouri 63110, and [6]Department of Psychiatry, Yale School of Medicine, New Haven, Connecticut 06519

Neuronal and network-level hyperexcitability is commonly associated with increased levels of amyloid-β (Aβ) and contribute to cognitive deficits associated with Alzheimer's disease (AD). However, the mechanistic complexity underlying the selective loss of basal forebrain cholinergic neurons (BFCNs), a well-recognized characteristic of AD, remains poorly understood. In this study, we tested the hypothesis that the oligomeric form of amyloid-β (oAβ_{42}), interacting with α7-containing nicotinic acetylcholine receptor (nAChR) subtypes, leads to subnucleus-specific alterations in BFCN excitability and impaired cognition. We used single-channel electrophysiology to show that oAβ_{42} activates both homomeric α7- and heteromeric $\alpha7\beta2$-nAChR subtypes while preferentially enhancing $\alpha7\beta2$-nAChR open-dwell times. Organotypic slice cultures were prepared from male and female ChAT-EGFP mice, and current-clamp recordings obtained from BFCNs chronically exposed to pathophysiologically relevant level of oAβ_{42} showed enhanced neuronal intrinsic excitability and action potential firing rates. These resulted from a reduction in action potential afterhyperpolarization and alterations in the maximal rates of voltage change during spike depolarization and repolarization. These effects were observed in BFCNs from the medial septum diagonal band and horizontal diagonal band, but not the nucleus basalis. Last, aged male and female APP/PS1 transgenic mice, genetically null for the $\beta2$ nAChR subunit gene, showed improved spatial reference memory compared with APP/PS1 aged-matched littermates. Combined, these data provide a molecular mechanism supporting a role for $\alpha7\beta2$-nAChR in mediating the effects of oAβ_{42} on excitability of specific populations of cholinergic neurons and provide a framework for understanding the role of $\alpha7\beta2$-nAChR in oAβ_{42}-induced cognitive decline.

Key words: basal forebrain cholinergic neurons; medium afterhyperpolarization; neuronal intrinsic excitability; oligomeric amyloid-beta; single-channel electrophysiology; spatial reference memory

Significance Statement

Aberrant neural activity can occur years before amyloid-β (Aβ) plaque deposition. Recent evidence has shifted focus toward the epileptogenic potential of soluble, oligomeric forms of A$\beta_{1\text{-}42}$ (oAβ_{42}) and its role in Alzheimer's disease (AD)-related cognitive decline. This study provides insight into the underling mechanisms mediating oAβ_{42}-induced hyperexcitation in neurons particularly susceptible to degeneration in AD. Using single-channel and whole-cell patch-clamp recordings, we demonstrate the following: (1) oAβ_{42} interacts with $\alpha7\beta2$-containing nicotinic receptors, altering the intrinsic excitability of specific populations of basal forebrain cholinergic neurons; and (2) $\alpha7\beta2$-nAChR signaling contributes to spatial reference memory deficits in the APP/PS1 mouse model of AD. Together, these findings reveal a unique role for $\alpha7\beta2$-nAChR signaling during early, AD-related pathologic events.

Received Apr. 15, 2020; revised Nov. 3, 2020; accepted Nov. 15, 2020.

Author contributions: A.A.G., H.A. B.-N., and P.W. designed research; A.A.G., J.M.V., C.X.-J., M.T.G., and J.R. C. performed research; A.A.G., J.M.V., J.R.C., H.A. B.-N., and M.R.P. analyzed data; A.A.G. wrote the first draft of the paper; A.A.G., J.M.V., H.A. B.-N., M.R.P., and R.J.L. edited the paper; A.A.G., M.R.P., R.J.L., and P.W. wrote the paper; J.R.C. and M.R.P. contributed unpublished reagents/analytic tools.

This work was primarily supported by Arizona Biomedical Research Commission ADHS14-083003 to A.A.G., Arizona Alzheimer's Consortium to A.A.G., and Barrow Neurological Foundation endowment and capitalization funds to A.A.G. This work was also supported by the National Institutes of Health R21 AG067029 to A.A.G. and R01 DA 043567 to A.A.G. and P.W. and R01 DA042749 to P.W. We thank Jason A. Miranda and Dale J. Buskirk for critical feedback on the manuscript; and Linda M. Lucero for technical assistance with concatemer design and construction.

The authors declare no competing financial interests.

Correspondence should be addressed to Andrew A. George at Andrew.George@dignityhealth.org.

https://doi.org/10.1523/JNEUROSCI.0876-20.2020

Introduction

Alzheimer's disease (AD) is a neurodegenerative disease afflicting >50 million individuals worldwide (projected to be >130 million by 2050). AD is classically diagnosed using postmortem histopathological biomarkers of neuritic amyloid-β (Aβ) plaques and neuronal/glial fibrillary tangles of hyperphosphorylated tau protein (Scheltens et al., 2016; Jack et al., 2018). Attempted treatments targeting amyloid precursor protein (APP) processing and Aβ aggregates have failed (Nicoll et al., 2019; Panza et al., 2019), perhaps because of intervention too late in disease progression. This has revealed gaps in understanding of molecular and cellular-level changes underlying AD etiopathogenesis. Recent studies suggest that early changes in AD are triggered by a soluble, oligomeric form of A$\beta_{1\text{-}42}$ (oAβ_{42}) (Yang et al., 2017). This form is elevated early in AD and has been targeted in promising clinical trials (Jongbloed et al., 2015; Hey et al., 2018). Many factors contribute to cognitive decline in AD (Selkoe, 2002; Pereira et al., 2005; Nimmrich and Ebert, 2009). Prominently, basal forebrain cholinergic neurons (BFCNs) and their projections modulate circuitry involved in cognitive processing (Picciotto et al., 2012; Zaborszky et al., 2012; Mesulam, 2013) and degenerate during the mild-cognitive impairment phase of AD (Grothe et al., 2012). This neuronal loss also could account for degeneration of hippocampal and cortical regions receiving BFCN innervation, and associated memory deficits (Grothe et al., 2014; Schmitz et al., 2016; X. Q. Chen and Mobley, 2019; Hampel et al., 2019). However, triggers for BFCN neurodegeneration are unknown, as is the potential role of elevated oAβ_{42} in BFCN loss in early AD.

Network hyperexcitability is a feature of AD and has been reported in numerous mouse models of AD pathology (Minkeviciene et al., 2009; Vossel et al., 2013). Importantly, oAβ_{42}'s ability to alter neuronal and network-level function and, ultimately, cognition has been linked to functional interactions between oAβ_{42} and nicotinic acetylcholine receptors (nAChRs) containing the α7 subunit (α7*-nAChR) (Puzzo et al., 2008; Gulisano et al., 2019; van Goethem et al., 2019). In many brain regions, α7*-nAChRs mediate synaptic transmission and regulate intrinsic neuronal excitability (Kawai et al., 2002; Liu et al., 2013; Dao et al., 2014). In most regions, α7*-nAChRs are homomers containing only α7 subunits. However, a small fraction also contain β2 subunits ($\alpha7\beta2$-nAChR). These heteromeric $\alpha7\beta2$-nAChRs form functional receptors (Khiroug et al., 2002; Murray et al., 2012), are highly sensitive to functional modulation by Aβ (Liu et al., 2009, 2012), and are enriched in specific populations of cholinergic and noncholinergic neurons of the basal forebrain (Khiroug et al., 2002; Azam et al., 2003; Thinschmidt et al., 2005). Together, these findings suggest that selective expression of the $\alpha7\beta2$-nAChR subtype on BFCN neurons might underlie the pathologic effects of oAβ_{42} on modulation of BFCN function through heightened or maladaptive activation of α7*-nAChRs.

We find that, similar to the endogenous ligand acetylcholine (ACh), a pathophysiologically relevant concentration of oAβ_{42} (100 nM) (Yang et al., 2017) directly activates both human α7- and $\alpha7\beta2$-nAChR but preferentially enhances $\alpha7\beta2$-nAChR $\alpha7\beta2$-nAChR single-channel open-dwell times. Furthermore, we demonstrate that BFCNs chronically exposed to oAβ_{42} exhibit enhanced action potential firing rates, and altered BFCN action potential waveforms (reduced time to spike, accelerated action potential repolarization, and reduced action potential medium afterhyperpolarization [mAHP]). These alterations in the intrinsic mechanisms mediating BFCN excitability are normalized through pharmacological antagonism of α7*-nAChR or genetic deletion of the β2-nAChR subunit gene. Last, we demonstrate that oAβ_{42}/$\alpha7\beta2$-nAChR interactions likely reduce acquisition and retention of spatial reference memory, using the well-established APP/PS1 transgenic AD mouse model. This study is the first to demonstrate specific molecular and intrinsic-level mechanisms through which oAβ_{42} enhances BFCN excitability, and provides a potential explanation for the selective vulnerability of these neurons in early AD. These findings also expand on findings that neuronal activity is increased by Aβ, including oAβ_{42} (Walsh et al., 2002; Palop et al., 2007; Busche et al., 2008; Palop and Mucke, 2009) and suggest novel strategies to ameliorate cellular processes contributing to BFCN loss and cognitive impairment.

Materials and Methods

Construct encoding a human α7-nAChR subunit-mCherry fusion protein

Human α7-nAChR subunits were engineered to express the red fluorescent protein mCherry as a fusion protein. This allowed direct visualization of nAChR expression *in vitro*. Using a DNA synthesis approach (GeneArt, Thermo Fisher Scientific), the mCherry sequence was inserted between the native, human nAChR α7 subunit's second, large intracellular domain amino acid residues C412 and S413 (numbering from the translation start methionine), while avoiding interruption of post-translational modification and/or regulatory sequences (Nashmi et al., 2003). Correct modification was confirmed by DNA sequencing (Thermo Fisher Scientific). The nucleotide sequence of this mCherry-tagged α7-nAChR subunit was optimized for expression in vertebrate expression systems. Optimizations included minimization of high GC content sequence segments, improved codon usage, reduction of predicted RNA secondary structure formation, and removal of sequence repeats and possible alternative start and splice sites. This construct is referred to as "unlinked α7-nAChR-mCherry," to differentiate it from the concatenated α7*-nAChR constructs described next, and was subcloned into the mammalian expression vector pcDNA 3.1-Zeocin.

Construct for the nAChR chaperone NACHO

The human sequence for the α7*-nAChR chaperone protein NACHO (Gu et al., 2016) was subcloned into the bicistronic mammalian expression vector pIRES (Addgene), facilitating simultaneous, constitutive expression of both NACHO and the GFP ZsGreen1. This construct was engineered to facilitate the cell-surface expression of α7- and $\alpha7\beta2$-nAChR constructs and the visual identification of SH-EP1 cells expressing NACHO.

Constructs encoding concatenated homomeric α7 or heteromeric $\alpha7\beta2$-nAChR

Fully pentameric α7*-nAChR concatemers were constructed, encoding three different arrangements of subunits: 5′-α7-α7-α7-α7-α7-3′ [α7 concatemer], 5′-α7-α7-β2-α7-α7-3′ [$\alpha7\beta2$(P3) concatemer], or 5′-α7-β2-α7-β2-α7-3′ [$\alpha7\beta2$(P2,P4) concatemer]. These were engineered largely as previously described (George et al., 2017), with the exception that the nucleotide sequences for α7 subunit genes expressed in the fifth subunit position were modified to include the mCherry sequence, as described in the preceding section for the unlinked α7-nAChR-mCherry construct. All other features of the constructs, including linker lengths and composition, placement of unique restriction sites within the nucleotide sequences encoding these linkers, and positioning of Kozac, signal peptide, and stop sequences, are as described in our previous publication (George et al., 2017). Schematics of these linear constructs and their assembled format (including locations of agonist binding sites) are provided in Figure 1*A* and Figure 1*B*, respectively. Sequences of all subunits, together with their mCherry fluorophore and associated linkers, were confirmed by DNA sequencing (Thermo Fisher

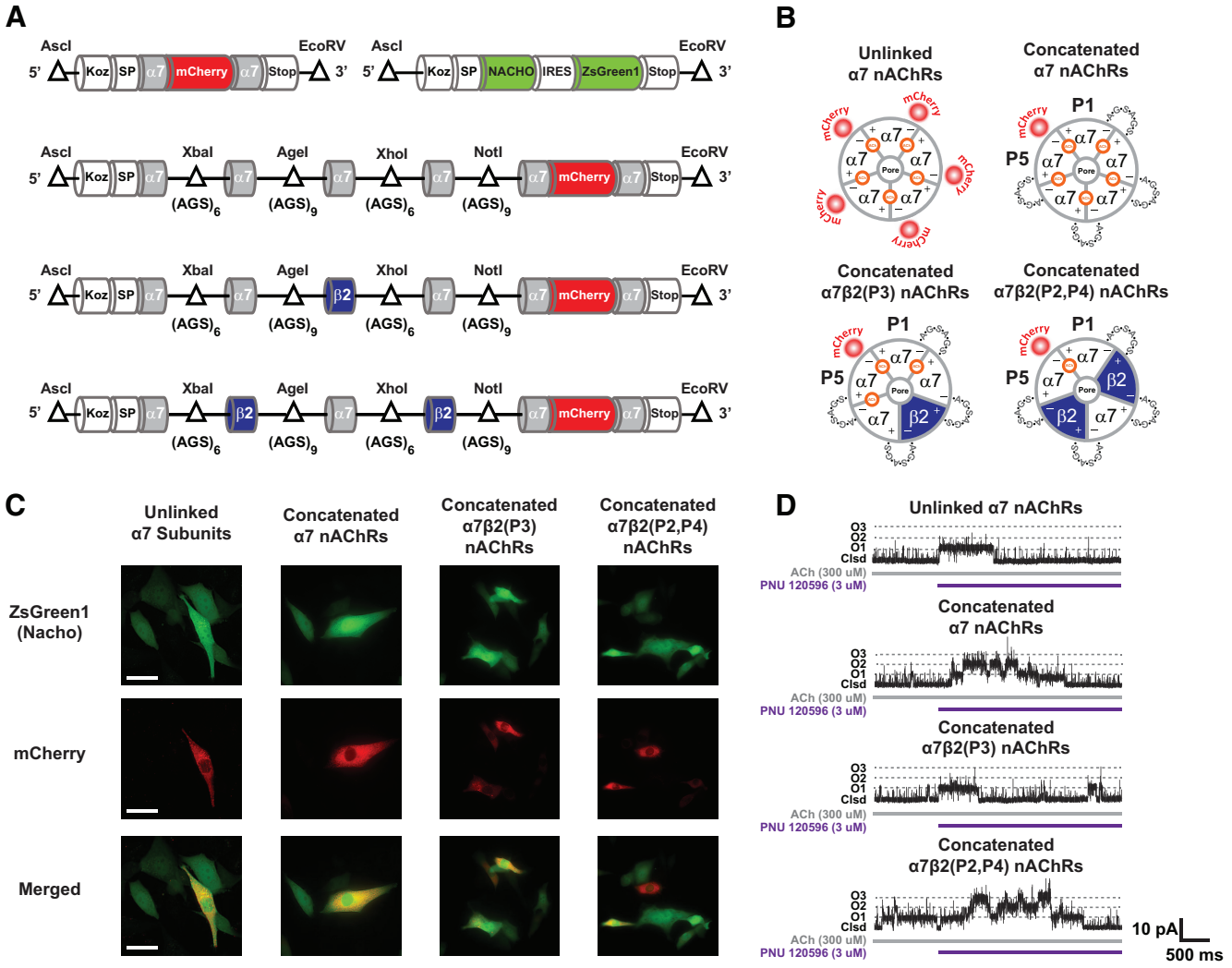

Figure 1. Design, engineering, and functional expression of human $\alpha7$- and $\alpha7\beta2$-nAChR. ***A***, Schematic illustration of $\alpha7$ and $\alpha7\beta2$-nAChR DNA constructs (from top to bottom): Single $\alpha7$ subunit gene ($\alpha7$ unlinked) fused to mCherry, nAChR chaperone protein NACHO coexpressed with ZsGreen1, concatenated $\alpha7$-nAChR (containing only $\alpha7$ subunits ($\alpha7$ homopentamer); $\alpha7$-mCherry fusion in position 5) concatenated $\alpha7\beta2$(P3)-nAChR (containing a single $\beta2$ subunit in position 3; $\alpha7$-mCherry fusion in position 5), and concatenated $\alpha7\beta2$(P2,P4)-nAChR (containing two $\beta2$ subunits in position 2 and 4; $\alpha7$-mCherry fusion in position 5). ***B***, Illustration of assembly and stoichiometry of unlinked $\alpha7$-nAChR homopentamer, concatenated $\alpha7$-nAChR homopentamer, concatenated $\alpha7\beta2$(P3)-nAChR, and concatenated $\alpha7\beta2$(P2,P4)-nAChR. ***C***, Fluorescent imaging of $\alpha7$- and $\alpha7\beta2$-nAChR constructs transiently expressed in SH-EP1 cell lines. Top panels, NACHO expression (ZsGreen1). Middle panels, $\alpha7$*-nAChR expression (mCherry). Bottom panels, Cells coexpressing NACHO and $\alpha7$*-nAChR (merged; yellow). ***D***, Cell-attached single-channel responses from $\alpha7$- and $\alpha7\beta2$-nAChR. Single-channel responses were elicited with ACh (300 μM; gray bar below each representative trace). Closed (Clsd) and open receptor states (O1-O3; dashed lines) are indicated for each nAChR subtype. Perfusion of the $\alpha7$-selective PAM PNU 120596 during ACh application (3 μM; purple bar below each representative trace) enhances $\alpha7$- and $\alpha7\beta2$-nAChR single-channel activity, producing longer-lasting bursts of openings.

Scientific), and correct assembly of each translated pentamer was verified at the cDNA level by restriction digest. These validated, fully pentameric, concatenated $\alpha7$- and $\alpha7\beta2$-nAChR-mCherry constructs were subcloned into the mammalian expression vector pcDNA 3.1-Zeocin. As shown by our published work (Moretti et al., 2014), concatenated $\alpha7$- or $\alpha7\beta2$-nAChR form functional receptors that recapitulate pharmacological and single-channel functional properties of native $\alpha7$*- and $\alpha7\beta2$-nAChR (Fu and Jhamandas, 2003; Andersen et al., 2016; Corradi and Bouzat, 2016; Bouzat and Sine, 2018; Nielsen et al., 2018).

Cell culture

The unmodified SH-EP1 human epithelial cell line (nAChR null) was maintained as previously described (Fryer and Lukas, 1999; Eaton et al., 2014). Briefly, DMEM (high glucose, bicarbonate-buffered, with 1 mM sodium pyruvate and 8 mM L-glutamine) was supplemented with 10% horse serum, 100 U/ml penicillin, 100 µg/ml streptomycin, and 0.25 µg/ml amphotericin B (Invitrogen) plus 5% FBS (Hyclone) on 100-mm-diameter plates in a humidified atmosphere containing 5% CO_2 in air at 37°C. SH-EP1 cells were passaged once per week as described previously (Lukas, 1993; Eaton et al., 2003) and maintained at 80% confluence.

Transient transfection SH-EPI cells

Forty-eight hours before transfection, SH-EP1 cells were split (1:50) and plated on 35 mm cell culture dishes coated with poly-D-lysine. NACHO-ZsGreen1 and nAChR-mCherry cDNA constructs (unlinked $\alpha7$-nAChR subunits, $\alpha7$-nAChR concatemer, $\alpha7\beta2$(P3)-nAChR concatemer, or $\alpha7\beta2$(P2,P4)-nAChR concatemer) were cotransfected at a 1:1 ratio (1 µg NACHO cDNA: 1 µg nAChR cDNA) using QIAGEN's Effectene transfection kit. Following transfection, cells were incubated at 37°C for 2 d in complete DMEM without antibiotic selection. On the day of single-channel recordings, cells were rinsed twice with prewarmed extracellular solution (described in Preparation of oAβ_{42}) to remove residual DMEM and allowed to equilibrate at 22°C for 5 min before recording.

Preparation of oAβ_{42}

Preparation of synthetic human or mouse oAβ_{42} strictly adhered to methods previously described (Stine et al., 2011). Briefly, 1 mM Aβ stock

solutions were made by solubilizing lyophilized human or mouse A$\beta_{1\text{-}42}$ powder (California Peptide Research) in 1,1,1,3,3,3-hexafluoro-2-propanol. Aβ peptide films were stored over desiccant in glass jars at −20°C. Before use, A$\beta_{1\text{-}42}$ peptide films were removed from −20°C freezer and warmed to 22°C. oAβ_{42} was prepared under sterile conditions by resuspension of A$\beta_{1\text{-}42}$ peptide films in DMSO and sonicated for 10 min before dilution in cold ACSF (for single-channel recordings) or neurobasal media (for organotypic basal forebrain slice preparations) to a final stock concentration of 100 μM. Samples were vortexed (15 s), spun down, and transferred to 4°C for 24 h. To avoid protofibril formation, samples were not used for more than the day of a given experiment. This protocol yields oAβ_{42} based on the evaluation of similarly prepared samples via negative-staining electron and atomic force microscopy (Liu et al., 2013).

Native/PAGE Western blotting to validate Aβ_{42} oligomers

To confirm the preservation of oAβ_{42} assemblies in basal forebrain organotypic slice cultures, basal forebrain organotypic cultures were prepared from male and female ChAT-EGFP mice (P7) as described above and exposed to neurobasal media containing 100 nM oAβ_{42} at 37°C. Neurobasal media containing oAβ_{42} was harvested immediately after exposure (time point 0; T0) and after a 24 h exposure period (time point 24; T24). Western blot analysis was performed to on samples from T0 and T24 to determine the predominant form(s) of Aβ (see Fig. 5*G*). Native PAGE for oAβ_{42} assemblies was performed using a 12-well 4%-12% RunBlue Bis-Tris gels (Expedeon) under native conditions with 8 μl of media loaded per lane using a Tris-glycine running buffer. Independent samples of media were used at T0 and T24. Nitrocellulose blots were probed with mouse-anti-APP/Aβ (m6E10; BioLegend), followed by a sheep anti-mouse antibody conjugated to peroxidase (Cytiva). Bands were detected with Lumigen-TMA6 (GE Healthcare) and captured digitally using the Kodak ImageStation 440CF. Densitometry was performed using the Kodak 1D Image Analysis software.

Single-channel electrophysiology

Cells cotransfected with both the α7- or $\alpha7\beta2$-nAChR constructs and the chaperone protein NACHO were selected for recording. These appeared yellow under fluorescence microscopy because of coexpression of the red mCherry and ZsGreen1 tags associated with the nAChR and NACHO constructs, respectively (illustrated in Fig. 1*C*). Single-channel α7- and $\alpha7\beta2$-nAChR-mediated currents were recorded from SH-EPI cells under cell-attached configuration similar to that previously described for nAChR single-channel recordings from *Xenopus laevis* oocytes (George et al., 2017; Weltzin et al., 2019). All single-channel recordings were performed at room temperature (22°C). Patch pipettes were fabricated from thick-walled borosilicate glass (WPI), and tips were microforged to a final resistance of 15-20 MΩ. To elicit single-channel events, patch pipettes were filled with extracellular solution containing the following (in mM): 119 NaCl, 2.5 KCl, 1.25 NaH_2PO_4, 24 $NaHCO_3$, 12.5 glucose, 2 $CaCl_2{\cdot}4H_2O$, 2 $MgSO_4{\cdot}7H_2O$, and 1.5 atropine) that contained either ACh, corresponding to EC_{50} values for each construct (α7- and $\alpha7\beta2$-nAChR constructs = 300 μm) (Moretti et al., 2014) or oAβ_{42} (100 nM; falling within the range of pathophysiologically relevant concentrations previously described in humans) (Yang et al., 2017) and in rodent models of AD (Fá et al., 2016; Koppensteiner et al., 2016). The concentrations of ACh and oAβ_{42} used in our study were based, in part, on the practical consideration of choosing a concentration of oAβ_{42} that resulted in the robust single-channel activation of both α7- or $\alpha7\beta2$-containing nAChR without resulting in open-channel blockade of either receptor subtype. Patch pipettes also contained 100 nM charybdotoxin to block endogenous large conductance (BK) voltage and Ca^{2+}-dependent potassium channels. These ACh and oAβ_{42} concentrations produced sufficient open-channel events for analysis without producing an excessive overlap of unitary events or open-channel blockade of receptors (which can occur in the presence of very high agonist concentrations) (Papke and Oswald, 1989). Recordings were performed using an Axopatch 200B amplifier (Molecular Devices). For quality control, patches with seal resistance <10 GΩ were immediately discarded. Patches were clamped at a transmembrane potential of 100 mV. Current recordings were sampled at 50 kHz using pClamp10.7 (Molecular Devices) and low-pass filtered at 10 kHz. A Gaussian digital filter with a final cutoff frequency of 5 kHz was used during analysis. All single-channel recordings were analyzed using QuB software (version 1.4.0.132; https://qub.mandelics.com/). QuB software was used for preprocessing, which included baseline correction and idealization of single-channel events according to a half-amplitude, threshold-crossing criterion (George et al., 2017; Weltzin et al., 2019).

Experimental design

Promptly on seal formation, single-channel events (elicited by ACh or oAβ_{42}) were recorded for 15 min before bath perfusion (rate = 200 µl/s) of the nonselective nAChR antagonist mecamylamine (Meca; 1 mM) or the competitive antagonist methyllycaconitine (MLA; 10 nM, an α7*-nAChR-selective concentration). Single-channel recordings proceeded in the presence of Meca or MLA for an additional 15 min before the same patches were exposed to the Type II, α7*-nAChR-specific, positive allosteric modulator (PAM), PNU 120596 for an additional 5 min to validate α7- or $\alpha7\beta2$-nAChR single-channel events. Single-channel events were recorded for an additional 5 min in the presence of PNU 120596 before termination of the recording. ACh or oAβ_{42}-elicited single-channel events from α7- or $\alpha7\beta2$-nAChR could be sustained for ~30 min before observing significant rundown in single-channel activity in the absence of PNU 120596.

Single-channel openings from α7- or $\alpha7\beta2$-nAChR exhibit a broad distribution of current amplitudes that mainly result from limited time resolution of the inherently brief α7 and/or $\alpha7\beta2$ openings (Andersen et al., 2013; Nielsen et al., 2018). However, these single-channel events may also represent a subpopulation of distinct subconductance states (Andersen et al., 2013). To define the conductance state for α7- and $\alpha7\beta2$-nAChR constructs used in this study, we used the α7-specific PAM PNU-120596 to isolate the main conductance state for both α7- and $\alpha7\beta2$-nAChR. Amplitude stability plots were generated from single-channel events elicited in the presence of ACh & PNU-120596 or oAβ_{42} & PNU-120596 for α7-containing (linked and concatenated) nAChR (main amplitude of 4.8 ± 0.02 pA and 4.5 ± 0.03 pA; elicited with ACh or oAβ_{42}, respectively), $\alpha7\beta2$(P3) nAChR (main amplitude of 5.2 ± 0.03 pA and 6.8 ± 0.06 pA; elicited with ACh or oAβ_{42}, respectively), and $\alpha7\beta2$(P2,P4) nAChR (main amplitude of 4.7 ± 0.02 pA and 6.6 ± 0.08 pA; elicited with ACh or oAβ_{42}, respectively). Single-channel bursts corresponding to these precise amplitudes were segregated from isolated openings and only bursts were used for single-channel analysis (described below).

All recordings were analyzed using a Gaussian digital filter with a final cutoff frequency of 5 kHz. Single-channel amplitudes were derived from the idealized trace by fitting the raw data to a simple closed–open (C↔O) kinetic model. Closed- and open-dwell time distributions were generated for each recording and fitted by the sum of exponential functions by maximum likelihood. Closed-dwell time distributions were best fit with four components, and open-dwell time distributions were best fit with two components. Bursts of single-channel activity were defined as a series of openings separated by closures shorter than the minimum interburst closed duration (or T_{crit}) and separated from others by closed times longer than T_{crit} (Colquhoun and Sakmann, 1985). For all groups tested, the minimum interburst closed duration, or T_{crit}, was calculated using QuB software. Bursts containing overlapping currents, which indicate two simultaneously active channels, were rare and were discarded from analysis. The advantage of using bursts was to unequivocally determine that all the openings in a burst come from the same individual channel, and that the closed-dwell times within bursts can be interpreted in terms of channel mechanisms, even under conditions where there is an unknown number of channels in the patch. Under these conditions, no single-channel bursts were observed in untransfected SH-EP1 cells, which were exposed to ACh or oAβ_{42}, or in SH-EPI cells that were doubly transfected with any of the α7- or $\alpha7\beta2$-nAChR constructs together with NACHO, but recorded from in the absence of ACh or oAβ_{42}.

Single-channel closed-dwell times were determined from individual patches, and time constants for each closed- and open-dwell time

component were averaged across multiple patches. Averaged closed- and open-dwell times for each nAChR construct were compared in the presence of ACh or oAβ_{42}. Single-channel stability plots for amplitudes and closed- and open-dwell time distributions were determined for each individual patch, and means for single-channel amplitudes and open-dwell times were compared in the presence of ACh or oAβ_{42}. To determine whether oAβ_{42} performed as an allosteric modulator at α7- and/or $\alpha7\beta$2-nAChR, both ACh (300 μM) and oAβ_{42} (100 nM) were added to the pipette simultaneously. For each group, single-channel burst durations were pooled from multiple patches. Single-channel open-dwell time distributions were generated from bursts of single-channel activity only, and therefore did not include isolated openings. All burst open-dwell time histograms were best fit with 2 exponentials as previously described (George et al., 2017). Each individual exponential and their respective time constants (τ) for single-channel open-dwell times were calculated using Qub software. Time constants of each exponential (i.e., short and long burst durations) were compared between α7- and $\alpha7\beta$2-nAChR constructs in the presence of ACh or oAβ_{42}.

Single-channel electrophysiology statistical analysis. Group data for single-channel burst rates (bursts/s) and open-dwell times (τ values; ms) were analyzed using one-way ANOVA with Tukey's *post hoc* test for multiple comparisons. Two-way ANOVA was used (statistical significance set at $p < 0.05$) to compare differences in burst rates among all α7*-nAChR and between ACh and oAβ_{42} and followed by a Tukey's *post hoc* test for multiple comparisons where applicable (GraphPad software). Data are mean ± SEM.

Basal forebrain organotypic slice preparations. Basal forebrain organotypic slice cultures were prepared according to methods previously described (Stoppini et al., 1991; Ting et al., 2014; Buendia et al., 2016). Initially, brains were removed from ChAT(BAC)-EGFP and nonlittermate β2 nAChR subunit KO mice (of either sex; postnatal day 7; see Animal husbandry, breeding, and safeguards) and placed immediately in ice-cold cutting solution composed of the following (in mM): 92 NaCl, 2.5 KCl, 1.2 NaH_2PO_4, 30 $NaHCO_3$, 20 HEPES, 25 glucose, 5 sodium ascorbate, 2 thiourea, 3 sodium pyruvate, 10 $MgSO_4{\cdot}7H_2O$, 0.5 $CaCl_2{\cdot}2H_2O$, 100 kynurenic acid, and 100 U/ml penicillin and 0.100 mg/ml streptomycin. Organotypic slices containing the medial septum diagonal band (MSDB), horizontal diagonal band (HDB), or nucleus basalis (NB) were sectioned at 400 µm and immediately placed in ice-cold neurobasal media [supplemented with 25% heat-inactivated horse serum, ascorbic acid (500 μM)], 2 mmol/l L-glutamine, B-27 supplement and NGF (Sigma Millipore, 10 ng/ml), and 100 U/ml penicillin and 0.100 mg/ml streptomycin. Slices were transferred to Millicell 0.4 μm culture inserts within each well of a six-well culture tray containing neurobasal media supplemented with B-27 and NGF in the presence or absence of oAβ_{42} (100 nM). As a control, a scrambled version of the oAβ_{42} peptide was prepared following the same methodology as the oligomeric isoform (methods strictly adhering to Stine et al., 2011). To avoid protofibril formation, neurobasal media containing oAβ_{42} or scrambled oAβ_{42} were exchanged every 24 h. Basal forebrain organotypic slices were incubated at 37°C with 5% CO_2 for 9 d before whole-cell patch-clamp recordings.

Whole-cell patch-clamp electrophysiology. Basal forebrain organotypic slice cultures were transferred from Millicell inserts to a recording chamber perfused with oxygenated ACSF composed of the following (in mM): 124 NaCl, 2.5 KCl, 1.2 NaH_2PO_4, 24 $NaHCO_3$, 5 HEPES, 13 glucose, 2 $MgSO_4{\cdot}7H_2O$, 2 $CaCl_2{\cdot}2H_2O$ (osmolarity 300-310; pH 7.3) and maintained at room temperature throughout the experiment. BFCNs were identified under epifluorescence illumination using a BX50-WI Olympus microscope with a 40× water immersion objective. BFCNs from ChAT-EGFP transgenic mice were identified within the MSDB, HDB, and NB based on their neuroanatomical location and functional expression of EGFP. Additional features (e.g., low firing frequency, lack of membrane potential sag, and prominent spike AHP) were consistently associated with this neuronal population and were used to provide further validation of their neuroanatomical location and distinct electrophysiological characteristics (Liu et al., 2009; Unal et al., 2012; McKenna et al., 2013; Hedrick et al., 2016). BFCNs from β2 nAChR subunit KO mice were identified based on their neuroanatomical location, soma size (>25 µm), and distinct electrophysiological characteristics (above), all of which matched those of neurons positively identified in the ChAT-EGFP line.

For whole-cell recordings, patch pipettes were microforged to a final resistance of 8-10 MΩ and were filled with the following (in mM): 135 K-gluconate, 10 HEPES, 2 $MgCl_2$, 0.5 $CaCl_2$, 2 Mg-ATP, 0.1 Na-GTP, 10 phosphocreatine, and 5 EGTA, pH 7.3. Current-clamp recordings were corrected for 11.8 mV liquid junction potential between the intracellular and recording solutions (Neher, 1992). All voltage signals were amplified using an Axopatch 200B patch-clamp amplifier and digitized at a rate of 50 kHz (DigiData1440A, Molecular Devices). BFCNs were current-clamped at −65 mV, and access resistance was continuously monitored during recordings using pClamp10 software. To eliminate the contribution of spontaneous excitatory and inhibitory synaptic inputs onto BFCNs, recordings were performed in the presence of the synaptic blockers CNQX (25 μM in ACSF), AP-5 (50 μM in ACSF), and gabazine (SR-95 531 hydrobromide at 10 μM in ACSF), all purchased from Tocris Bioscience.

Experimental design

BFCN resting membrane potential (RMP, mV) was measured in current-clamp mode at I = 0, and RMP was measured immediately after whole-cell formation. To assess the effects of oAβ_{42} exposure on BFCN intrinsic activity, we initially presented BFCNs with a ramp current injection (0.1 pA/ms; 1 s) from a constant holding command of −65 mV. We used this ramp protocol to determine action potential threshold, latency to first spike, and maximal rates of voltage change (dV/dt_{max}) during spike depolarization and repolarization. Next, we presented BFCNs with a step current injection protocol (−100 pA to 100 pA; δ level: 20 pA, duration: 1 s) to examine BFCN firing rates and input resistance. Last, we used a single-step current injection protocol (500 pA; duration: 1 s) to measure BFCN mAHP.

BFCN firing rates were averaged for each current injection amplitude, and comparisons were drawn across experimental groups for each current injection between 20 and 100 pA. The mAHP (mV) amplitude was defined as the difference between baseline and the AHP potential measured 100 ms after cessation of the current stimulus, averaged across individual recordings, and measured from the baseline before the AP burst. Phase-plane portraits were generated for each BFCN by deriving the membrane potential with respect to time (dV/dt) and plotting it as a function of BFCN membrane potential. The maximal rate of voltage change (dV/dt_{max}) was measured during spike depolarization and repolarization for each of the first 10 action potentials generated using the ramp current-injection protocol and then averaged across BFCNs within each forebrain nucleus. Action potential threshold was experimentally determined and defined by the membrane potential at which dV/dt of the first action potential of the phase plane plot crossed 20 mV/ms (Yu et al., 2008). The maximal rate of voltage change (dV/dt_{max}) during spike depolarization and repolarization was calculated for the first 10 action potentials generated during the ramp current-injection protocol. Action potentials were individually compared across groups. Latency to first spike was measured for each BFCN and defined as the period between the start of the recording and arrival at the first action potential threshold. Action potential amplitude was defined as the peak voltage from threshold to the peak of the action potential. Passive membrane properties (Table 1) were measured from MSDB, HDB, and NB BFCNs during each experimental condition (i.e., scrambled oAβ_{42} control, oAβ_{42} alone, MLA + oAβ_{42}, and β2 nAChR KO slices + oAβ_{42}). Cell capacitance (pF) was determined using pClamp's automatic whole-cell compensation function. BFCNs were excluded from further analysis if the RMP > −55 mV or if the access resistance fluctuated >10%. Input resistance was measured by calculating the slope of the voltage change in response to current injections ranging from −100 pA to −20 pA (δ level = 20 pA).

Whole-cell patch-clamp electrophysiology statistical analysis. Comparisons of BFCN firing rates and mAHP amplitudes were

evaluated across all groups using one-way ANOVA followed by a Tukey's *post hoc* test for multiple comparisons. Differences in dV/dt_{max} across groups were analyzed using two-way ANOVA with statistical significance set at $p < 0.05$, followed by a Tukey's *post hoc* test for multiple comparisons. Action potential threshold, time to first spike, and action potential amplitude were analyzed using one-way ANOVA with Tukey's *post hoc* test (GraphPad software). Data are mean ± SEM.

Animal husbandry, breeding, and safeguards. All procedures were performed in accordance with the National Institutes of Health's *Guide for the care and use of laboratory animals* and institutional guidelines established by the Animal Care and Use Committee at the Barrow Neurologic Institute. Mice were maintained in standard housing on a 12 h light/dark cycle. C57BL/6J WT male and female mice expressing enhanced GFP under the control of the ChAT promoter (ChAT(BAC)-EGFP, The Jackson Laboratory; stock #007902), male and female $\beta2$ nAChR subunit KO mice [$\beta2$ nAChR KO; generously provided by Marina Picciotto, Yale University (Picciotto et al., 1995)], male and female APP/PS1-129/SvJ [generously provided by Drs. Antonella Caccamo and Salvatore Oddo; Arizona State University; (Caccamo et al., 2017)] were used. The latter two lines were used to generate mice used for behavioral testing (see below).

Generation of mice used for whole-cell patch-clamp recordings and Morris water maze (MWM) behavioral testing. For whole-cell patch-clamp recordings, ChAT(BAC)-EGFP and $\beta2$ nAChR KO colonies used were each maintained through homozygous × homozygous mating. For MWM, generation of $\beta2$ nAChR KO, APP/PS1, and APP/PS1-$\beta2$ nAChR KO mice was accomplished by backcrossing APP/PS1-129/SvJ mice (heterozygous for APP/PS1 transgene) to $\beta2$ nAChR KO/C57Bl6 mice for 10 generations to produce the following littermates: $\beta2$ nAChR KO mice, APP/PS1 mice, and APP/PS1-$\beta2$KO mice on a defined C57Bl6 background. The resulting littermates could be genotyped as follows: (A) hemizygous for the APP/PS1 transgene and genetically null for $\beta2$ nAChR subunit expression (i.e., APP/PS1-$\beta2$KO-C57Bl6), (B) hemizygous for the APP/PS1 transgene and homozygous for $\beta2$ nAChR subunit expression (i.e., APP/PS1-C57Bl6), or (C) absent of the APP/PS1 transgene and homozygous for $\beta2$ nAChR subunit expression (i.e., $\beta2$ nAChR KO-C57Bl6). As an additional control, WT 129/SvJ mice were backcrossed with WT C57Bl6 mice (i.e., $\beta2$ positive-C57Bl6) for the same number of generations to control for strain differences.

Genotyping. Genomic DNA was isolated from ear punches (postnatal day 21) using Phire Animal Tissue Direct PCR Kit (Thermo Fisher Scientific). For $\beta2$ nAChR subunit gene expression, male and female mice were genotyped using primers specific for $\beta2$ nAChR subunit gene expression and the β-galactosidase transgene (LacZ) (Picciotto et al., 1995) as follows: Lac-Z reaction primers (Lac-Z-5′: CAC TAC GTC TGA ACG TCG AAA ACC CG) and (Lac-Z-3′: CGG GCA AAT ATC GGT GGC CGT GG); for $\beta2$ reaction primers as follows: (B2-5′: CGG AGC ATT TGA ACT CTG AGC AGT GGG GTC GC) and (B2-3′: CTC GCT GAC ACA AGG GCT GCG GAC); for PS1 transgene reaction primers as follows (PS1-5′: AAT AGA GAA CGG CAG GAG CA) and (PS1-3′: GCC ATG AGG GCA CTA ACA T). Mice positive for the APP/PS1 transgene showed a product of 650 bp. Mice homozygous for $\beta2$ nAChR subunit expression showed a product at 650 bp (β-galactosidase transgene) and 350 bp ($\beta2$ nAChR expression). Animals lacking LacZ expression while positive for $\beta2$ nAChR expression (i.e., heterozygous) were excluded from behavioral testing.

MWM. Spatial reference memory was tested using a modified version of the MWM as previously described (M. T. Williams et al., 2003; Koebele et al., 2019). Briefly, mice (males and females; aged 10 months) were tested in a circular tub (188 cm in diameter) filled with water (22°C) tinted with white, nontoxic paint. Animals were randomized into groups to be placed in the maze from one of four cardinal locations (North, South, East, or West). Using visual cues, mice then had 60 s to locate a platform, which was submerged 1.5 cm beneath the surface of the water and remained in a fixed location in the southwest quadrant. Data acquisition was performed using a video camera mounted on the ceiling, and swim path was recorded and analyzed using EthoVision XT tracking software (Noldus Information Technology).

Experimental design

Spatial reference memory. Animals were tested from four cohorts, each representing a unique genotype (described above). If a mouse failed to find the platform that was located in the southwest quadrant within 60 s, it was guided to the platform and maintained on the platform for 15 s before being placed into a heated cage until the following trial. Mice received 4 trials/day for 6 consecutive days, with an intertrial interval of ~10 min. A fifth probe trial was administered on day 6 in which the platform was removed to evaluate whether the mice used spatial cues to locate the platform. Latency and distance to the platform were measured for each genotype and compared across days. For the probe trial, target quadrant frequency (frequency of crossings into platformed quadrant) and percent of the total swim distance in the target quadrant (% of total) were compared with the quadrant diagonally opposite (northeast) and follow methods previously described (Bimonte-Nelson et al., 2015). To reassociate the original platform location with escape, a seventh trial was given, identical to Trials 1-4. Further, we assessed the effects of $\beta2$ nAChR subunit expression on overnight forgetting by comparing latency to the platform from the last test trial on the first day (Trial 4 on day 1) to the first test trial the next day (Trial 1 on day 2), and for the overnight interval from day 2 to 3, etc. (Braden et al., 2010).

Visible platform test. Following spatial reference memory testing, animals were given a visual platform test to rule out the possibility that the observed spatial learning deficits were a product of impaired vision or abnormal motor function necessary to solve a water-escape maze task. Mice were given six trials/platform location with the platform location varied across three different locations. Mice were dropped off from the same location across trials. Animals remained on the platform for 15 s after finding the platform before being placed back into a heated cage before the subsequent trial (intertrial interval of ~10 min).

MWM statistical analysis. Behavioral data were evaluated using two-way ANOVAs with statistical significance set at $p < 0.05$, followed by a Fisher's LSD *post hoc* correction for multiple comparisons where applicable (StatView software). Omnibus repeated-measures ANOVAs, with one level repeated (day of testing) and one level between subjects (genotype), were used as a statistical measure for MWM training sessions. Differences in MWM probe test behavior were tested using two-way ANOVA followed by a Fisher's LSD multiple comparisons test and using Student's *t* test to compare within groups (GraphPad Software). Data are mean ± SEM.

Results

Single-channel electrophysiological recordings of ACh-induced openings of α7- and α7β2-nAChR can be obtained consistently from transiently-transfected SH-EP1 cells

We used a single-channel recording strategy, using transiently transfected, native nAChR-null, human SH-EP1 cells expressing concatenated human homomeric $\alpha7$- or heteromeric $\alpha7\beta2$-nAChR (Fig. 1*A*,*B*) to determine whether oAβ_{42} modulation of $\alpha7$- or $\alpha7\beta2$-nAChR is dependent on the position and stoichiometric arrangement of $\alpha7$ and $\beta2$ subunits within functional pentamers.

To validate these cells for single-channel electrophysiological experiments, we first stimulated with ACh at 300 μM, a typical EC_{50} concentration for homomeric $\alpha7$- and heteromeric $\alpha7\beta2$-nAChR (Moretti et al., 2014). Cells visualized under fluorescence microscopy to coexpress nAChR-mCherry and NACHO-ZsGreen1 (Gu et al., 2016; Matta et al., 2017) were chosen and consistently expressed functional $\alpha7$*-nAChR responding to ACh (Fig. 1*C*). Single-channel openings were seen as typical bursts of activation (examples shown in Fig. 1*D*) interspersed within longer periods of inactivity (corresponding to closed or desensitized states) (Nielsen et al., 2018). Channel openings also

typically had a range of amplitudes and were short-lived. Because the latter could lead to underestimates of conductance state(s), and conductance state determinations could be confounded by simultaneous openings of more than one channel per patch, we chose to analyze openings only of the lowest-amplitude state (O1) consistently observed throughout this study because this could be guaranteed to correspond to a unitary conductance. Moreover, recordings done in the presence of bath-applied PNU 120596 (3 μM) aided determination of the amplitude of O1 by enhancing single-channel open probability and open-dwell times (Fig. 1*D*), as previously noted (Lasala et al., 2019).

We next used a pharmacological approach to determine whether openings elicited by ACh were genuinely produced by activation of α7- or $\alpha7\beta2$-nAChR. Example data from individual patches are shown in Figure 2*A–C*. Single-channel events for each construct tested could be induced by ACh (300 μM) and could be suppressed by application of either the nonselective nAChR antagonist Meca (1 mM; Fig. 2*A*) or the α7*-nAChR selective antagonist MLA (10 nM; Fig. 2*B*). In either case, subsequent application of the α7*-selective PAM PNU 120596 enabled recovery of function, even in the presence of Meca or MLA. These results show that single-channel responses of human, heterologously expressed α7-nAChR formed from loose or linked subunits, or of human $\alpha7\beta2$-nAChR heterologously expressed as two isoforms from concatenated subunits, are all similarly activated by exposure to ACh. Sensitivity to functional blockade by either Meca or MLA, or restoration of responses by PNU 120596 all demonstrate that the effects of ACh in this system are mediated via human α7*-nAChR.

oAβ_{42} directly activates α7- and $\alpha7\beta2$-nAChR

To address the lack of consensus about functional interactions between oAβ_{42} and α7*-nAChR, we began by conducting single-channel recordings of SH-EP1 cells expressing human homomeric α7- or heteromeric $\alpha7\beta2$-nAChR that were exposed to oAβ_{42} (100 nM) in the patch pipette (Fig. 2*D*,*E*). We used exactly the same pharmacological approach as applied to the analysis of ACh-induced responses to demonstrate that these oAβ_{42}-evoked single-channel events also correspond to activation of α7*-nAChR. Similar to ACh exposure, oAβ_{42}-induced responses could be blocked by bath application of either Meca or MLA (Fig. 2*D* and Fig. 2*E*, respectively). Receptor function suppressed by Meca- or MLA-mediated blockade of oAβ_{42}-induced single-channel activity was restored by bath application of PNU 120596 (Fig. 2*A*,*B* and 2*D*,*E*, respectively).

To quantify the outcomes shown in typical traces for ACh-induced (Fig. 2*A–C′*) and oAβ_{42}-induced (Fig. 2*D–F′*) α7*-nAChR single-channel openings, a summary of data pooled across multiple patches containing homomeric α7- or heteromeric $\alpha7\beta2$-nAChR isoforms is shown in Figure 3. Exposure to Meca (1 mM) significantly reduced the single-channel burst rate in the presence of ACh for all α7*-nAChRs tested (Fig. 3*A*). Further, for all α7*-nAChR isoforms studied, application of PNU 120596, subsequent to block by Meca alone, resulted in the recovery of ACh-induced single-channel bursting to a level indistinguishable from that before Meca administration. Similar results were observed for ACh-induced single-channel responses in the presence of MLA (Fig. 3*B*). Perfusion of MLA significantly reduced (>90%) single-channel burst rates in the presence of ACh for all α7*-nAChR isoforms, whether expressed as unlinked or concatenated subunits. Further, for all α7*-nAChR isoforms studied, application of PNU 120596 subsequent to block by Meca alone, resulted in the recovery of single-channel activity and bursting rates to be statistically indistinguishable to those before MLA application. Since MLA and PNU 120596 had to be prepared in a DMSO solution, we also tested whether DMSO at the final concentration used in these experiments (0.002% v/v; vehicle control) had any effect on bursting rate (Fig. 3*C*). No differences in single-channel burst rates were observed for unlinked α7, concatenated α7, concatenated $\alpha7\beta2$(P3), or concatenated $\alpha7\beta2$(P2, P4) nAChR. Following DMSO application, the addition of PNU 120596 increased bursting rate significantly over that induced by ACh alone.

Comparable to the results observed for ACh, perfusion of Meca (1 mM) significantly reduced the single-channel burst rate in the presence of oAβ_{42} for all α7*-nAChR isoforms tested (Fig. 3*D*; >85% suppression). Furthermore, application of PNU 120596, subsequent to block by Meca alone, resulted in the recovery of single-channel bursting to a level indistinguishable from that before Meca administration. Nearly equivalent results were observed for oAβ_{42}-induced responses in the presence of MLA (Fig. 3*E*). MLA significantly reduced (>85%) single-channel burst rates in the presence of oAβ_{42} for all α7*-nAChR constructs. Further, for all α7*-nAChR isoforms studied, application of PNU 120596 subsequent to block by Meca alone resulted in the recovery of single-channel activity and bursting rates to be statistically indistinguishable to those before MLA application. Similar to the effects observed for ACh, no differences in single-channel burst rates were observed for unlinked α7, concatenated α7, concatenated $\alpha7\beta2$(P3), or concatenated $\alpha7\beta2$(P2,P4) nAChR in the presence of DMSO (0.002% v/v). Again, following DMSO application, the addition of PNU increased bursting rate significantly over that induced by oAβ_{42} alone. Furthermore, an analysis of burst rate of all α7*-nAChR subtypes before drug application revealed no main effect of ligand (i.e., ACh vs oAβ_{42}), and no significant interaction was observed between construct and ligand. These results indicate that both ACh versus oAβ_{42} are equally efficacious in activating the α7*-nAChR subtypes.

Next, we determined whether differences in single-channel burst rates were observed among α7*-nAChR subtypes tested or whether oAβ_{42} differentially altered single-channel burst rates compared with ACh. A main effect of construct on single-channel burst rate was observed ($F_{(3,32)} = 113.3$; $p = 0.00004$). Further, we show that there is no main effect of ligand ($F_{(1,32)} = 3.3$; $p = 0.08$). Nor was a significant interaction observed between construct and ligand ($F_{(3,32)} = 0.32$; $p = 0.81$). These results indicate that ACh versus oAβ_{42} are equally efficacious in activating the α7*-nAChR subtypes tested in this study. However, these experiments do not directly address whether oAβ_{42} acts as a traditional agonist or as allosteric modulator. To address this question, we coapplied ACh (300 μM) and oAβ_{42} (100 nM) to patches expressing α7- and $\alpha7\beta2$-nAChR subtypes. Interestingly, the coapplication of ACh and oAβ_{42} enhanced the single-channel burst rate of both α7- and $\alpha7\beta2$-containing nAChR ($F_{(3,37)} = 31.3$; $p = 0.00006$). *Post hoc* analyses indicate that the coapplication of ACh and oAβ_{42} increased the single-channel burst rate of both the α7 and $\alpha7\beta2$(P2,P4) concatenated nAChR compared with ACh alone (24.9 ± 1.6 to 63.0 ± 7.3, $p = 0.00008$ and 37.5 ± 2.1 to 75.8 ± 9.1, $p = 0.00005$; respectively) or oAβ_{42} alone (18.8 ± 1.8 to 63.0 ± 7.3, $p = 0.00003$ and 33.1 ± 2.1 to 75.8 ± 9.1, $p = 0.00009$;

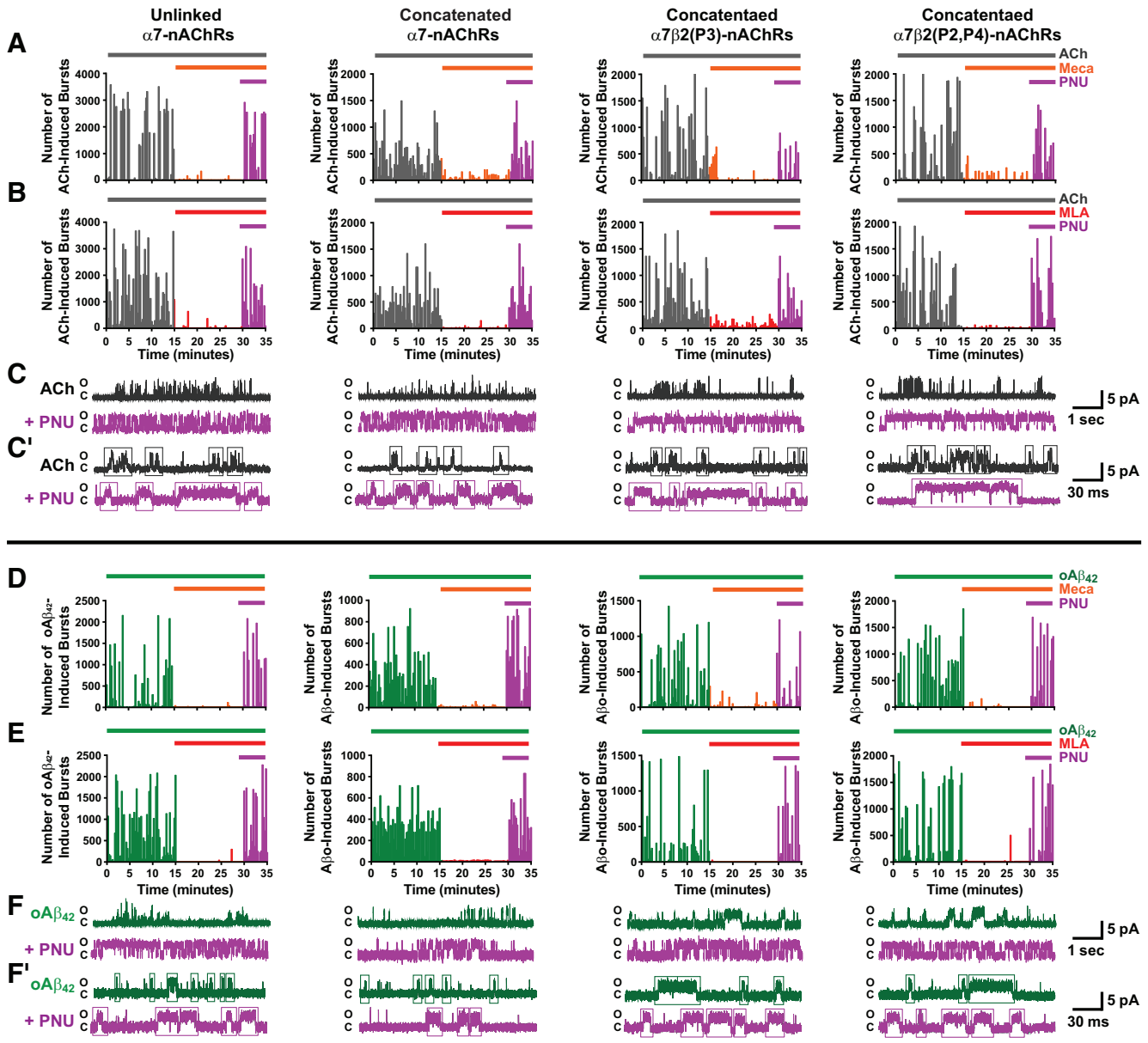

Figure 2. ACh and oAβ_{42} evoke similar single-channel activated bursts from α7- and $\alpha7\beta2$-nAChR. ***A***, Representative recordings of the frequency of cell-attached single-channel bursts elicited with ACh (300 μM) from unlinked homomeric α7-nAChR, concatenated homomeric α7-nAChR, concatenated $\alpha7\beta2$(P3)-nAChR, and concatenated $\alpha7\beta2$(P2,P4)-nAChR. ACh is administered throughout the recording, via the patch pipette. Horizontal lines within each panel indicate the duration of Meca administration (orange line indicates 1 mM; bath administration at 15 min) and PNU 120596 (purple line indicates 3 μM; bath administration at 30 min). ***B***, Same as in ***A***, except with bath application at 15 min of MLA (red line indicates 10 nM). ***C***, Representative traces of single-channel recordings from each of the four α7*-nAChR populations, responses elicited with ACh (gray traces) and verified with PNU 120596 administration (ACh + PNU; purple traces). ***C′***, High-resolution images of single-channel recordings for each of the four α7*-nAChR elicited with ACh and verified with PNU 120596. Examples of single-channel bursts are boxed in each trace. Bursts were segregated from isolated events, and only bursts were used in all single-channel analyses. ***D***, Representative recordings of the frequency of cell-attached single-channel bursts elicited with oAβ_{42} (100 nM) from unlinked homomeric α7-nAChR, concatenated homomeric α7-nAChR, concatenated $\alpha7\beta2$(P3)-nAChR, and concatenated $\alpha7\beta2$(P2,P4)-nAChR. oAβ_{42} is administered throughout the recording, via the patch pipette. Horizontal lines within each panel indicate the duration of Meca administration (orange line indicates 1 mM; bath administration at 15 min) and PNU 120596 (purple line indicates 3 μM; bath administration at 30 min). ***E***, Same as in ***D***, except with bath application at 15 min of MLA (red indicates 10 nM). ***F***, Representative traces of single-channel recordings from each of the four α7*-nAChR populations, elicited with oAβ_{42} (green traces) and verified with PNU 120596 administration (oAβ_{42} + PNU; purple traces). ***F′***, High-resolution images of single-channel recordings for each of the four α7*-nAChR elicited with oAβ_{42} and verified with PNU 120596. Single-channel bursts are boxed in each trace. These bursts were segregated from isolated events and only bursts were used in all single-channel analyses.

respectively). Collectively, these results demonstrate functional activation of human α7- and $\alpha7\beta2$-nAChR by oAβ_{42} as well as by ACh. Both Meca and MLA-mediated blockade, and restoration of function in the continued presence of antagonists by PNU 120596 support direct actions of oAβ_{42} at α7*-nAChR. The lack of an effect of DMSO at the assay concentration used (0.002%) verifies that all of the observed outcomes are induced by administration of ACh, oAβ_{42}, or drug, but not vehicle.

oAβ_{42} preferentially enhances the single-channel open-dwell times of $\alpha7\beta2$-nAChR

Having demonstrated that oAβ_{42} can directly activate α7- and $\alpha7\beta2$-nAChR subtypes, we next examined whether the open-dwell times of oAβ_{42}-evoked single-channel events were similar to or different from those induced by the canonical agonist ACh. Single-channel open-dwell time distributions for all homomeric α7-nAChR and heteromeric $\alpha7\beta2$-nAChR constructs were best

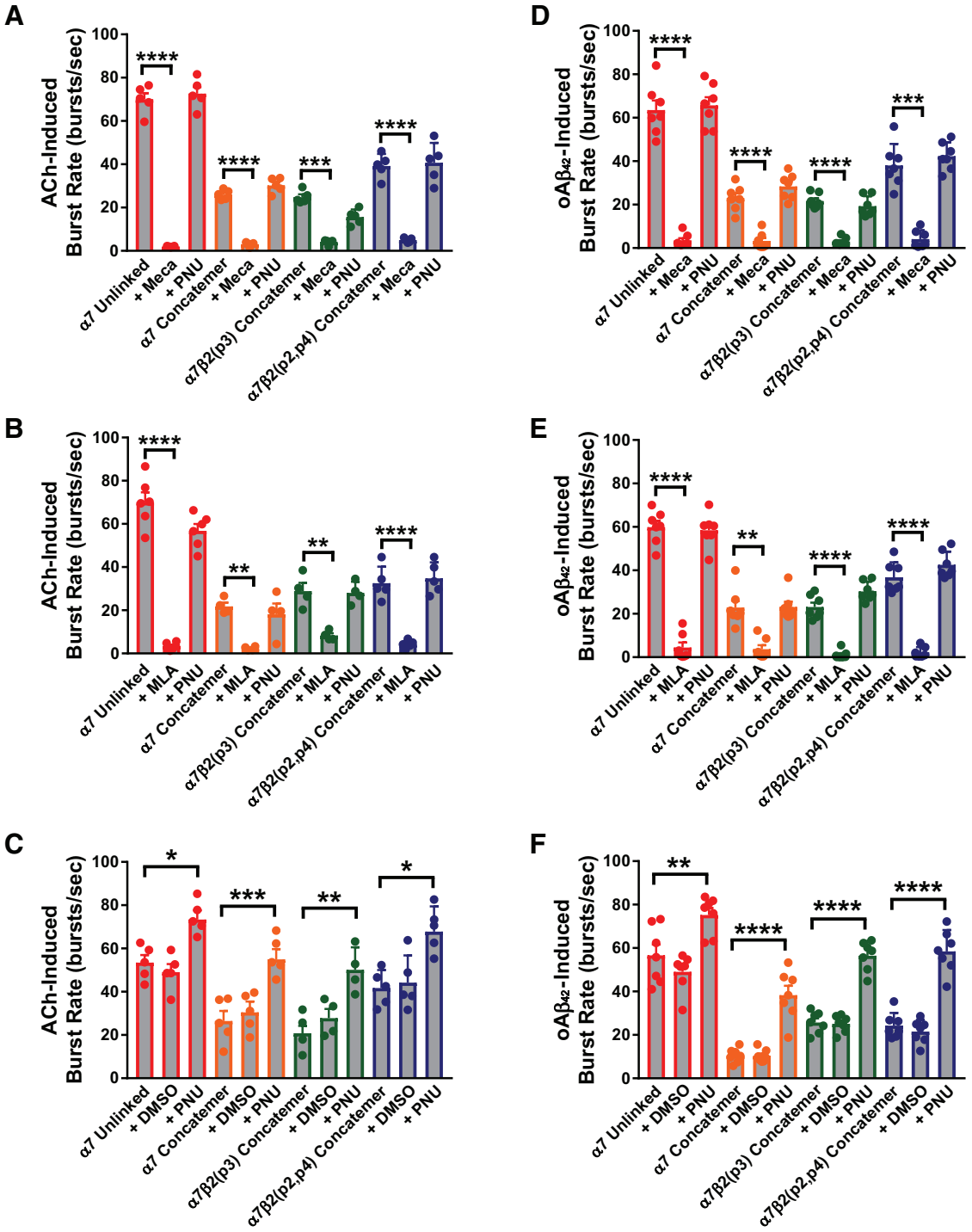

Figure 3. Analysis of ACh- and oAβ_{42}-induced single-channel burst rates. ***A***, Single-channel burst rates (bursts/s) in the presence of ACh (300 μM) were calculated for patches containing unlinked homomeric α7-nAChR (red), concatenated homomeric α7-nAChR (orange), concatenated $\alpha7\beta2$(P3)-nAChR (green), and concatenated $\alpha7\beta2$(P2,P4)-nAChR (blue). Burst rates were recorded under the following experimental conditions: before Meca application, during Meca (1 mM) application simultaneously with ACh stimulation, and during coapplication of both Meca and PNU 120596 (3 μM) simultaneously with ACh stimulation. Application of Meca significantly reduced the mean single-channel burst rates in the presence of ACh for all α7*-nAChR populations investigated: unlinked α7-nAChR homopentamers (69.9 $\pm$ 2.9 to 2.0 $\pm$ 0.1; $p = 0.00006$; $n = 5$), concatenated α7-nAChR homopentamers (26.0 $\pm$ 1.0 to 3.0 $\pm$ 0.4; $p = 0.00004$; $n = 5$), concatenated $\alpha7\beta2$(P3)-nAChR (24.8 $\pm$ 1.3 to 4.0 $\pm$ 0.5; $p = 0.00003$; $n = 5$), and concatenated $\alpha7\beta2$(P2,P4)-nAChR (39.2 $\pm$ 2.5 to 4.9 $\pm$ 0.4; $p = 0.00008$; $n = 5$). Subsequent coapplication of PNU 120596 with Meca to the same patches reversed the effects of Meca blockade. ACh-induced single-channel burst rates were returned to values indistinguishable from those before Meca was applied for all α7*-nAChR populations studied: α7-nAChR (unlinked α7-nAChR = 72.6 $\pm$ 3.1, $p = 0.73$; concatenated α7-nAChR = 30.2 $\pm$ 1.6, $p = 0.54$) and $\alpha7\beta2$-nAChR ($\alpha7\beta2$(P3)-nAChR = 15.6 $\pm$ 1.6, $p = 0.51$; $\alpha7\beta2$(P2,P4) = 40.7 $\pm$ 4.1 $p = 0.92$). ***B***, Same as in ***A***, except with the selective α7*-nAChR antagonist MLA (10 nM). Similar to Meca, MLA significantly reduced the ACh-induced single-channel burst rate for unlinked α7-nAChR (70.1 $\pm$ 4.6 to 3.4 $\pm$ 0.7, $p = 0.00002$, $n = 6$), concatenated α7-nAChR (21.8 $\pm$ 1.8 to 2.3 $\pm$ 0.4, $p = 0.005$, $n = 4$), concatenated $\alpha7\beta2$(P3)-nAChR (28.9 $\pm$ 3.8 to 8.3 $\pm$ 1.1, $p = 0.003$, $n = 4$), and concatenated $\alpha7\beta2$(P2,P4) nAChR (32.5 $\pm$ 3.5 to 4.3 $\pm$ 0.8, $p = 0.00006$, $n = 5$). Subsequent coapplication of MLA and PNU 120596 to the same patches reversed the MLA-induced reductions in burst rate, returning rates to levels indistinguishable from those before MLA was applied: unlinked α7-nAChR = 56.8 $\pm$ 3.2, $p = 0.76$; concatenated α7-nAChR = 18.1 $\pm$ 5.0, $p = 0.68$; concatenated $\alpha7\beta2$(P3)-nAChR = 28.1 $\pm$ 2.6, $p = 0.98$; concatenated $\alpha7\beta2$(P2,P4)-nAChR = 34.8 $\pm$ 3.3 $p = 0.83$). ***C***, Same as in ***A***, ***B***, except with DMSO (vehicle) control (0.002%) instead of antagonist (Meca or MLA) application. No differences in mean single-

fit with two open-dwell time components. This indicates the existence of two distinct populations of single-channel open durations in all cases, regardless of whether unlinked or concatenated nAChR subunit constructs were used (Fig. 4). This was true whether the openings were induced by ACh (Fig. 4*A*) or oAβ_{42} (Fig. 4*B*).

An analysis of the open-dwell time distributions of homomeric α7-nAChR (whether expressed from unlinked or concatenated subunits) revealed that single-channel open-dwell times for the shorter-duration population (τ1) evoked by either ACh or oAβ_{42} were indistinguishable (Fig. 4*C*). Similarly, no differences in duration were observed for the longer-duration population of single-channel (τ2) openings in the presence of ACh versus oAβ_{42}. However, the heteromeric $\alpha7\beta2$-nAChR presented a more complex picture. For $\alpha7\beta2$(P3)- or $\alpha7\beta2$(P2, P4)-nAChR, τ1 values (corresponding to the populations of shorter openings) were indistinguishable whether evoked by ACh or oAβ_{42}. However, τ2 values (corresponding to the populations of longer openings) were significantly extended in the presence of oAβ_{42} compared with ACh (Fig. 4*D*; 3.1- and 3.9-fold, respectively). Together with the findings shown in Figure 3, these data unequivocally demonstrate that oAβ_{42} activates both homomeric α7- and heteromeric $\alpha7\beta2$-nAChR, and that it alters $\alpha7\beta2$-nAChR kinetics by prolonging $\alpha7\beta2$-nAChR open-dwell times compared with those evoked by the conventional agonist, ACh. Last, we determined whether coapplication of ACh and oAβ_{42} altered the open-dwell times of α7*-nAChR, and we coapplied ACh (300 μM) and oAβ_{42} (100 nM) to patches expressing concatenated α7- and $\alpha7\beta2$-nAChR subtypes. Coapplication of ACh and oAβ_{42} failed to modulate the single-channel open-dwell times of either α7 ($\tau1 = 0.192 \pm 0.04$ ms, $p = 0.99$, $\tau2 = 1.7 \pm 0.33$ ms, $p = 0.99$) or $\alpha7\beta2$(P2,P4)-concatenated nAChR ($\tau1 = 0.224 \pm 0.03$ ms, $p = 0.99$, $\tau2 = 4.1 \pm 0.36$ ms, $p = 0.99$) compared with the single-channel open-dwell time elicited by oAβ_{42} alone. In the case of the $\alpha7\beta2$-nAChR, we would expect competitive antagonism to produce three distinct time constants (corresponding to short bursts produced by both ligands, medium duration bursts produced by ACh, and longer bursts produced by oAβ_{42}). Given these results, we conclude that oAβ_{42} acts as ago-PAM (i.e., an agonist working through an allosteric site that is also capable of acting as a PAM in the presence of an agonist) at $\alpha7\beta2$-containing nAChR. Since burst durations produced by both ligands at α7-nAChRs are indistinguishable, it remains an open question whether oAβ_{42} also acts as an ago-PAM at this subtype.

Subnucleus-specific enhancement of BFCN excitability is mediated by oAβ_{42}/$\alpha7\beta2$-nAChR interactions

The ability of Aβ to destabilize neuronal function has been well documented (Palop et al., 2007; Busche et al., 2012; Vossel et al., 2017). However, there is an inadequate understanding of (1) the molecular processes triggering BFCN dysfunction in response to elevations in oAβ_{42} and (2) how BFCNs transition from stable neuronal activity to hyperactive dysfunction. First, we determined whether the interaction between oAβ_{42} and α7*-nAChR leads to alterations in BFCN intrinsic excitability. We prepared basal forebrain organotypic slice cultures from ChAT-EGFP transgenic mice (postnatal day 7). These slices contained cholinergic neuronal populations from the MSDB (Fig. 5*A*), HDB (Fig. 5*B*), or the NB (Fig. 5*C*). Basal forebrain organotypic slices containing these nuclei were incubated for 9 d in oAβ_{42} (100 nM), scrambled oAβ_{42} (negative control; prepared under identical conditions to those used to prepare oAβ_{42}), oAβ_{42} (100 nM) + MLA (50 nM; used to block all α7*-nAChR function). Since no highly selective $\alpha7\beta2$-nAChR antagonist is available (Wu et al., 2016), organotypic slice cultures were also prepared from β2 nAChR KO mice to remove the possible contribution of $\alpha7\beta2$-nAChR from recordings. Organotypic slices from β2 nAChR KO mice were also incubated for 9 d in oAβ_{42} (100 nM). Following the 9 d incubation period, we used whole-cell current-clamp recordings and implemented a step current injection protocol (20 nA increments) using hyperpolarizing and depolarizing current pulses to measure voltage changes in BFCNs identified

←

channel burst rate were observed when moving from buffer only condition to the presence of the vehicle control for any of the α7*-nAChR constructs: unlinked α7-nAChR (54.4 ± 5.4 to 51.4 ± 3.2, $p = 0.9$, $n = 5$), concatenated α7-nAChR (26.5 ± 4.3 to 30.5 ± 5.0, $p = 0.75$, $n = 5$), concatenated $\alpha7\beta2$(P3)-nAChR (21.0 ± 4.5 to 26.5 ± 4.1, $p = 0.88$, $n = 4$) or concatenated $\alpha7\beta2$(P2,P4)-nAChR (40.9 ± 4.3 to 46.0 ± 4.8, $p = 0.56$, $n = 5$). Subsequent addition of PNU (3 μM) in the presence of the vehicle control increased single-channel burst rate significantly over those induced by ACh alone (α7 unlinked = 73.0 ± 2.6, $p = 0.011$, $n = 5$; α7 linked = 55.7 ± 2.8, $p = 0.0007$, $n = 5$; $\alpha7\beta2$(P3) = 52.5 ± 5.2 $p = 0.005$, $n = 4$; $\alpha7\beta2$(P2,P4) = 64.8 ± 5.4, $p = 0.012$, $n = 5$). ***D***, Single-channel burst rates (bursts/s) in the presence of oAβ_{42} (100 nM) were calculated for patches containing unlinked homomeric α7-nAChR (red), concatenated homomeric α7-nAChR (orange), concatenated $\alpha7\beta2$(P3)-nAChR (green), and concatenated $\alpha7\beta2$(P2,P4)-nAChR (blue). Burst rates were recorded under the following experimental conditions: before Meca application, during Meca (1 mM) application simultaneously with oAβ_{42} stimulation, and during coapplication of both Meca and PNU 120596 (3 μM) simultaneously with oAβ_{42} stimulation. Application of Meca significantly reduced the mean single-channel burst rates in the presence of oAβ_{42} for all α7*-nAChR populations investigated: unlinked α7-nAChR homopentamers (63.5 ± 4.4 to 3.4 ± 1.1; $p = 0.00003$; $n = 7$), concatenated α7-nAChR homopentamers (23.0 ± 2.2 to 3.3 ± 1.4; $p = 0.00001$; $n = 7$), concatenated $\alpha7\beta2$(P3)-nAChR (21.6 ± 1.3 to 3.0 ± 1.3; $p = 0.00003$; $n = 7$), and concatenated $\alpha7\beta2$(P2,P4)-nAChR (38.0 ± 3.8 to 4.1 ± 1.5; $p = 0.0003$; $n = 7$). Subsequent coapplication of PNU 120596 with Meca to the same patches reversed the effects of Meca blockade. oAβ_{42}-induced single-channel burst rates were returned to values indistinguishable from those before Meca was applied for all α7*-nAChR populations studied: α7-nAChR (unlinked α7-nAChR = 65.7 ± 3.8, $p = 0.63$; concatenated α7-nAChR = 28.4 ± 2.2, $p = 0.26$) and $\alpha7\beta2$-nAChR ($\alpha7\beta2$(P3)-nAChR = 19.3 ± 1.7, $p = 0.46$; $\alpha7\beta2$(P2,P4) = 42.3 ± 2.4 $p = 0.22$). ***E***, Mean oAβ_{42}-induced single-channel burst rates calculated for patches containing unlinked α7-nAChR, concatenated α7-nAChR, concatenated $\alpha7\beta2$(P3)-nAChR, and concatenated $\alpha7\beta2$(P2, P4)-nAChR before and after application of the selective α7*-nAChR antagonist MLA (10 nM). Similar to Meca, MLA significantly reduced the single-channel burst rate for unlinked α7-nAChR (59.9 ± 2.9 to 4.5 ± 2.3, $p = 0.00004$, $n = 7$), concatenated α7-nAChR (22.8 ± 3.2 to 3.7 ± 1.8, $p = 0.00003$, $n = 7$), concatenated $\alpha7\beta2$(P3)-nAChR (23.1 ± 2.0 to 1.2 ± 0.8, $p = 0.00004$, $n = 7$), and concatenated $\alpha7\beta2$(P2,P4)-nAChR (36.8 ± 2.6 to 2.2 ± 0.9, $p = 0.00002$, $n = 7$). Subsequent coapplication of MLA and PNU 120596 to the same patches reversed the MLA-induced reductions in burst rate, returning rates to levels indistinguishable from those before MLA was applied: unlinked α7-nAChR = 58.5 ± 2.9, $p = 0.13$; concatenated α7-nAChR = 23.2 ± 2.4, $p = 0.61$; concatenated $\alpha7\beta2$(P3)-nAChR = 30.3 ± 1.7, $p = 0.54$; concatenated $\alpha7\beta2$(P2,P4)-nAChR = 42.5 ± 2.3 $p = 0.58$). ***F***, Same as in ***A***, ***B***, except with DMSO (vehicle) control (0.002%) instead of antagonist (Meca or MLA) application. No differences in mean single-channel burst rate were observed when moving from buffer only condition to the presence of the vehicle control for any of the α7*-nAChR constructs: unlinked α7-nAChR (56.6 ± 4.9 to 49.0 ± 3.2, $p = 0.25$, $n = 7$), concatenated α7-nAChR (10.5 ± 1.2 to 10.3 ± 1.1, $p = 0.62$, $n = 7$), concatenated $\alpha7\beta2$(P3)-nAChR (25.7 ± 1.9 to 25.1 ± 1.5, $p = 0.5$, $n = 7$), or concatenated $\alpha7\beta2$(P2,P4)-nAChR (24.3 ± 2.2 to 21.5 ± 2.0, $n = 7$, $p = 0.56$). Subsequent addition of PNU (3 μM) in the presence of the vehicle control increased single-channel burst rate significantly over those induced by oAβ_{42} alone (α7 unlinked = 56.6 ± 25.0 to 75.2 ± 3.3, $p = 0.003$, $n = 7$; α7 linked = 10.5 ± 1.2 to 38.3 ± 4.3, $p = 0.00005$, $n = 7$; $\alpha7\beta2$(P3) = 25.7 ± 1.9 to 56.5 ± 2.6 $p = 0.00004$, $n = 7$; $\alpha7\beta2$(P2,P4) = 24.3 ± 2.2 to 58.5 ± 3.7, $p = 0.00006$, $n = 7$). For each group, n indicates individual patches. Bursts were segregated from isolated events, and only bursts were used in all single-channel analyses. All within-group comparisons were analyzed using one-way ANOVA with Tukey's *post hoc* test. Across-group comparisons between ACh and oAβ_{42} were analyzed using two-way ANOVA with Tukey's *post hoc* test. ***A–F***, Data are mean single-channel burst rate ± SEM. $*p < 0.05$, $**p < 0.01$, $***p < 0.001$, $****p < 0.0001$.

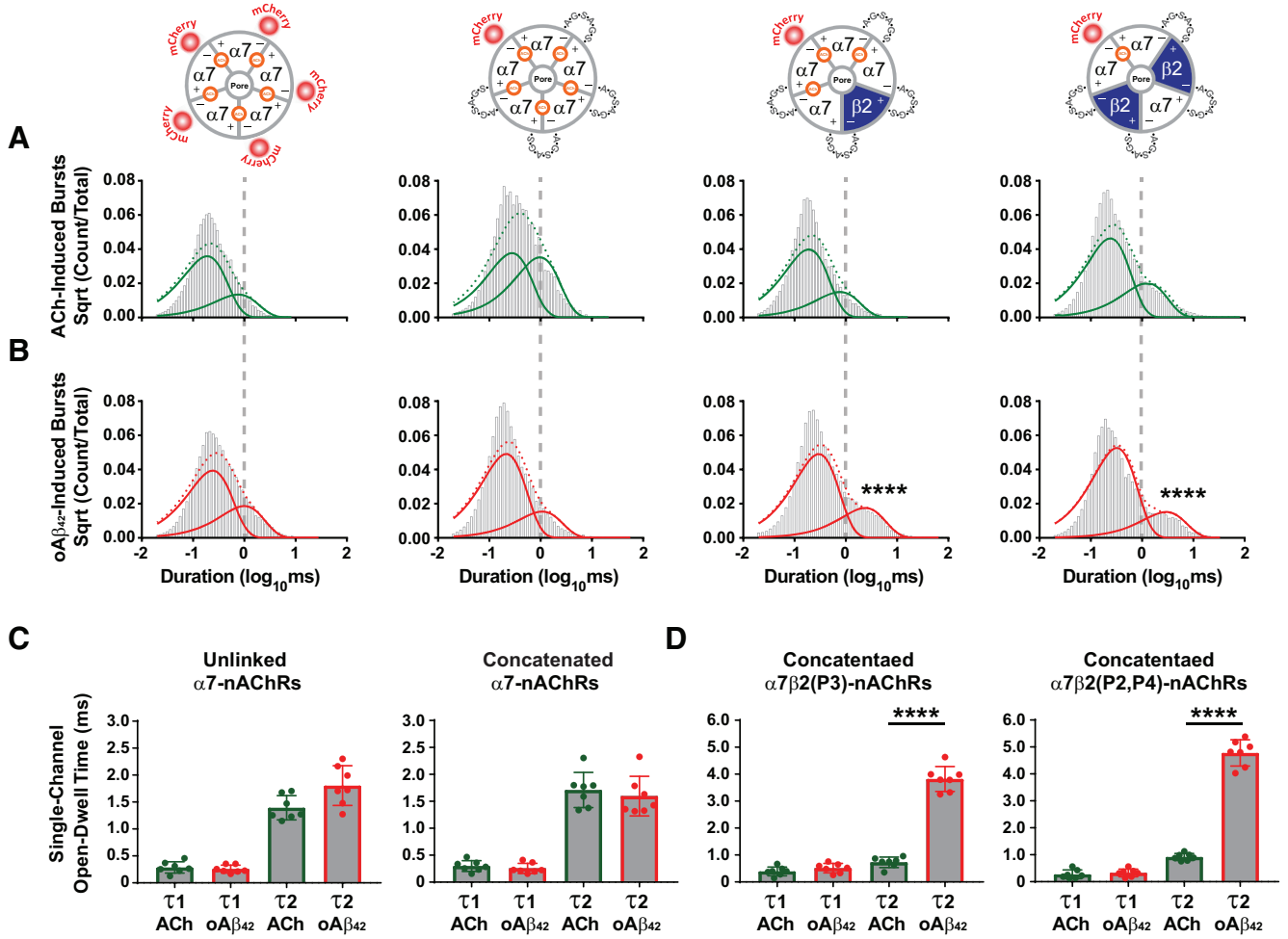

Figure 4. oAβ_{42} preferentially enhances single-channel open-dwell times of $\alpha7\beta2$-but not $\alpha7$-nAChR. Single-channel open-dwell time distributions generated for $\alpha7$ and $\alpha7\beta2$-nAChR activated by (***A***) ACh (300 μM) or (***B***) oA$\beta_{1\text{-}42}$ (100 nM). Single-channel open-dwell time distributions were best fit with 2 components for ACh-elicited single-channel bursts (solid green lines; dotted green line indicates overall fit) and oAβ_{42}-elicited single-channel bursts (solid red lines; dotted red line indicates overall fit). ***A***, ***B***, Vertical dashed lines indicate 1 ms open-dwell time duration, shown for reference. ***C***, Mean single-channel open-dwell times were calculated for each open time constant (τ) observed for homomeric $\alpha7$-nAChR in the presence of ACh or oAβ_{42}. No significant differences were seen in $\tau1$ values (corresponding to shorter-duration openings) that were induced by ACh versus oAβ_{42} (unlinked $\alpha7$-nAChR, $\tau1$ ACh = 0.3 ± 0.04 ms vs $\tau1$ oAβ_{42} = 0.26 ± 0.03 ms, $p = 0.93$, $n = 7$; concatenated $\alpha7$-nAChR, $\tau1$ ACh = 0.29 ± 0.04 ms vs $\tau1$ oAβ_{42} = 0.26 ± 0.04 ms, $p = 0.90$, $n = 7$). Nor were significant differences seen in $\tau2$ values (corresponding to longer-duration openings) that were induced by ACh versus oAβ_{42} (unlinked $\alpha7$-nAChR, $\tau2$ ACh = 1.4 ± 0.08 ms vs $\tau2$ oAβ_{42} = 1.8 ± 1.4 ms, $p = 0.74$, $n = 7$; concatenated $\alpha7$-nAChR, $\tau2$ ACh = 1.7 ± 0.12 ms vs $\tau2$ oAβ_{42} = 1.6 ± 0.14 ms, $p = 0.91$). One-way ANOVA summary: $F_{(3,24)}$ range 85.1-68.3, $p = 0.00008$. ***D***, Mean single-channel open-dwell times were also calculated for each open time constant (τ) observed for openings of heteromeric $\alpha7\beta2$-nAChR in the presence of ACh or oAβ_{42}. Shorter-duration single-channel open-dwell times (indicated by $\tau1$) evoked by the two ligands were indistinguishable for concatenated $\alpha7\beta2$(P3)- or $\alpha7\beta2$(P2,P4)-nAChR ($\alpha7\beta2$(P3), $\tau1$ ACh = 0.4 ± 0.06 ms vs $\tau1$ oAβ_{42} = 0.5 ± 0.06 ms, $p = 0.87$, $n = 7$; $\alpha7\beta2$(P2,P4), $\tau1$ ACh = 0.27 ± 0.06 ms vs $\tau1$ oAβ_{42} = 0.33 ± 0.05 ms, $p = 0.94$). However, oAβ_{42} significantly enhanced the longer-duration openings (indicated by $\tau2$) of concatenated $\alpha7\beta2$-nAChR isoforms ($\alpha7\beta2$(P3), $\tau2$ ACh = 0.7 ± 0.07 ms vs $\tau2$ oAβ_{42} = 3.8 ± 0.18 ms, $p = 0.0002$, $n = 7$; $\alpha7\beta2$(P2, P4), $\tau2$ ACh = 0.92 ± 0.05 ms vs $\tau2$ oAβ_{42} = 4.8 ± 0.18 ms, $p = 0.0007$). One-way ANOVA summary: $F_{(3,24)}$ range 245.1-430.6, $p = 0.00009$. Bursts were segregated from isolated events, and only bursts were used in all single-channel analyses. Individual data points represent mean open-dwell times for individual single-channel recordings. For each group, *n* indicates individual patches. All data analyzed using one-way ANOVA with Tukey's *post hoc* test. ***A-D***, Data are mean single-channel burst rate ± SEM. ****$p < 0.0001$.

within these three regions. Representative current-clamp recordings are shown for the four conditions specified (Fig. 5*A′–C′*), and group data for numbers of action potentials elicited are shown (Fig. 5*D–F*).

Within the MSDB, BFCNs chronically exposed to oAβ_{42} exhibited an increase in the number of action potentials generated across the entire range of depolarizing current injections compared with scrambled oAβ_{42} controls (Fig. 5*D*). The observed oAβ_{42}-induced increase in spike rate was normalized either through pharmacological antagonism of $\alpha7$*-nAChR with MLA or through genetic deletion of the $\beta2$ nAChR subunit. Similarly, organotypic slices incubated in oAβ_{42} showed enhanced HDB BFCN action potential firing rates for nearly all current injections compared with scrambled oAβ_{42} (Fig. 5*E*). Similar to MSDB neurons, inhibition of $\alpha7$- and $\alpha7\beta2$-nAChR with MLA or genetic deletion of the $\beta2$ nAChR subunit normalized the induced increase in HDB BFCN action potential firing rate compared with scrambled oAβ_{42} controls.

By contrast, BFCNs within NB that were exposed to oAβ_{42} exhibited no difference in spike number compared across NB BFCNs in organotypic slices incubated in scrambled oAβ_{42}, slices coincubated with oAβ_{42} + MLA, or $\beta2$ nAChR KO slices incubated with oAβ_{42} (Fig. 5*F*). As demonstrated by our single-channel studies (Fig. 2), activation by oAβ_{42} can persist for >30 min, compared with acute macroscopic activation induced by a bolus of conventional agonist (which typically persists for milliseconds) (D. K. Williams et al., 2011). Indeed, the typically accepted explanation for extended closed-dwell times between

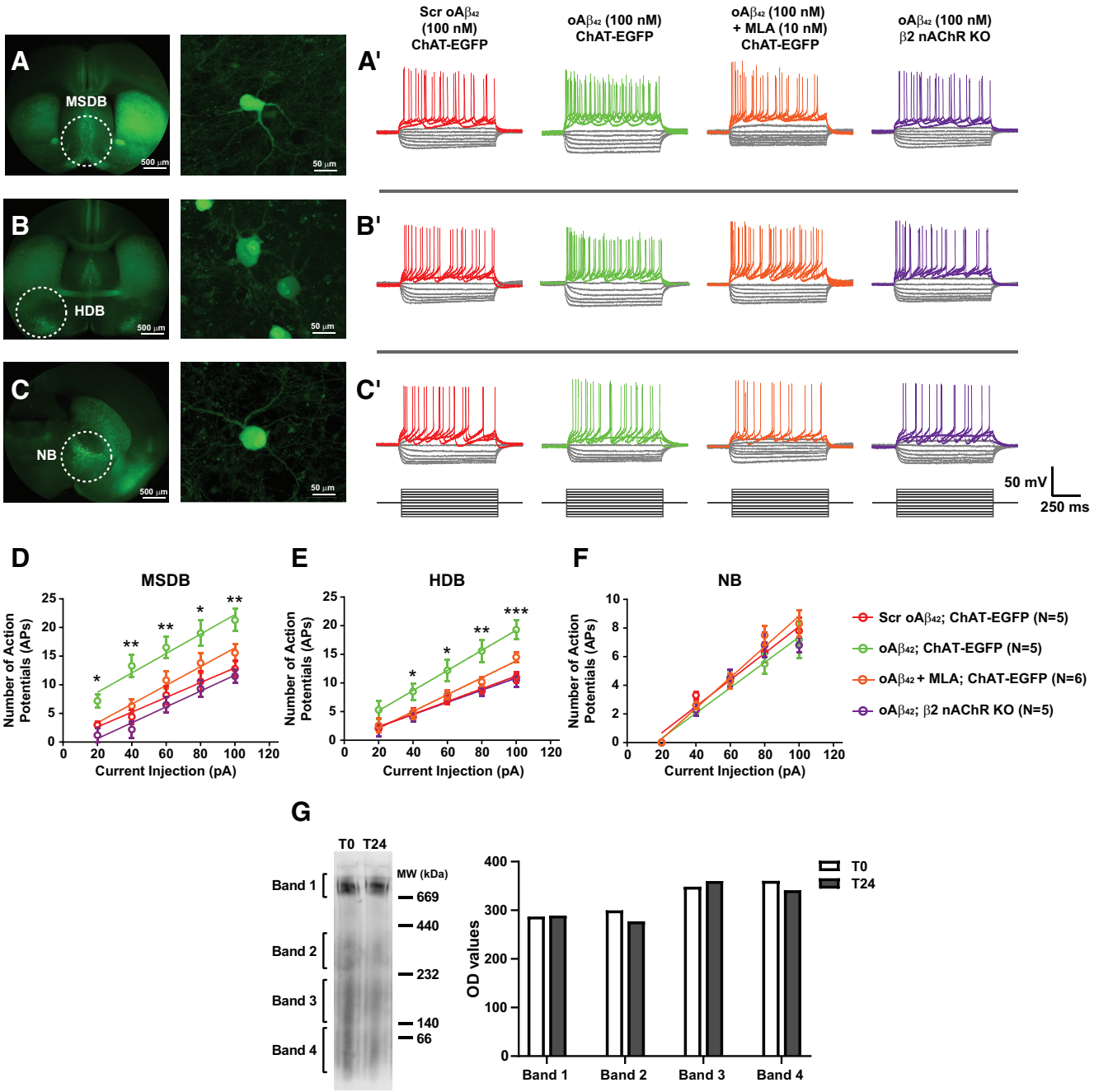

Figure 5. oAβ_{42} induces BFCN hyperexcitation through the activation of $\alpha7\beta2$-nAChR. ***A–C***, Organotypic basal forebrain slice cultures prepared from ChAT-EGFP transgenic mice. BFCNs were identified for patch-clamp recordings from the MSDB (dashed circle; ***A***), HDB (dashed circle; ***B***), and the NB (dashed circle, ***C***). ***A′-C′***, Representative current-clamp recordings from MSDB (***A′***), HDB (***B′***), and NB (***C′***) cholinergic neurons. A current step protocol (−100 to 100 pA; 20 pA steps; below representative traces) was applied to MSDB, HDB, and NB BFCNs that were chronically incubated with a scrambled version of oAβ_{42} (Scr; 100 nM; red), oAβ_{42} (100 nM; green), or oAβ_{42} + MLA (100 and 10 nM, respectively; orange). Organotypic slice cultures were also prepared from $\beta2$ nAChR subunit KO mice and incubated with oAβ_{42} (100 nM; purple). ***D***, MSDB BFCNs chronically exposed to oAβ_{42} exhibited a significant increase in the number of action potentials generated across the entire range of depolarizing current injections compared with scrambled oAβ_{42} controls (20 pA, oAβ_{42} = 7.2 ± 1.2 vs scrambled oAβ_{42} = 3.0 ± 0.6, $F_{(3,15)} = 7.6$, $p = 0.003$, Tukey's $p = 0.02$; 40 pA, oAβ_{42} = 13.3 ± 1.9 vs scrambled oAβ_{42} = 4.4 ± 1.2, $F_{(3,15)} = 10.2$, $p = 0.0006$, Tukey's $p = 0.003$; 60 pA, oAβ_{42} = 16.8 ± 1.9 vs scrambled oAβ_{42} = 8.2 ± 1.5, $F_{(3,15)} = 7.6$, $p = 0.003$, Tukey's $p = 0.008$; 80 pA, oAβ_{42} = 19.0 ± 2.3 vs scrambled oAβ_{42} = 10.6 ± 1.7, $F_{(3,15)} = 5.3$, $p = 0.011$, Tukey's $p = 0.026$; 100 pA, oAβ_{42} = 21.3 ± 1.9 vs scrambled oAβ_{42} = 12.8 ± 1.5, $F_{(3,15)} = 7.4$, $p = 0.003$, Tukey's $p = 0.006$; oAβ_{42}, $n = 12$; scrambled oAβ_{42} controls, $n = 12$). The observed oAβ_{42}-induced increase in action potential firing rate was reversed with MLA or through genetic deletion of the $\beta2$ nAChR subunit ($p > 0.05$ for all current injections; compared with scrambled oAβ_{42} controls; oAβ_{42} + MLA, $n = 10$; $\beta2$ nAChR KO slices incubated with oAβ_{42}, $n = 8$). ***E***, HDB BFCNs exposed to oAβ_{42} also exhibited enhanced action potential firing rates across nearly all current injections (20 pA, oAβ_{42} = 5.3 ± 1.6 vs scrambled oAβ_{42} = 2.1 ± 0.5, $F_{(3,16)} = 1.5$, $p = 0.26$, Tukey's $p = 0.29$; 40 pA, oAβ_{42} = 8.8 ± 1.4 vs scrambled oAβ_{42} = 4.3 ± 0.8, $F_{(3,16)} = 4.9$, $p = 0.014$, Tukey's $p = 0.033$; 60 pA, oAβ_{42} = 12.2 ± 1.8 vs scrambled oAβ_{42} = 7.0 ± 0.8, $F_{(3,16)} = 4.2$, $p = 0.025$, Tukey's *post hoc*, $p = 0.038$; 80 pA, oAβ_{42} = 15.6 ± 1.9 vs scrambled oAβ_{42} = 9.3 ± 0.8, $F_{(3,16)} = 6.6$, $p = 0.004$, Tukey's $p = 0.01$; 100 pA, oAβ_{42} = 19.3 ± 1.7 vs scrambled oAβ_{42} = 11.0 ± 0.9, $F_{(3,16)} = 11.1$, $p = 0.0003$, Tukey's $p = 0.0008$; oAβ_{42}, $n = 12$; scrambled oAβ_{42} controls, $n = 12$). Pharmacological antagonism with MLA or genetic deletion of the $\beta2$ nAChR subunit normalized this effect (Tukey's $p > 0.05$ for all current injections; compared with scrambled oAβ_{42} controls; oAβ_{42} + MLA, $n = 12$; $\beta2$ nAChR KO slices incubated with oAβ_{42}, $n = 10$). ***F***, NB BFCNs exposed to oAβ_{42} exhibited no differences in the number of action potentials generated under the same conditions compared with scrambled oAβ_{42} controls (20 pA, no spikes elicited for oAβ_{42} or scrambled oAβ_{42} groups; 40 pA, oAβ_{42} = 2.2 ± 0.3 vs scrambled oAβ_{42} = 3.3 ± 0.3, $F_{(3,16)} = 2.5$, $p = 0.10$, Tukey's $p = 0.11$; 60 pA, oAβ_{42} = 4.5 ± 0.5 vs Scrambled oAβ_{42} = 4.5 ± 0.5, $F_{(3,16)} = 0.03$,

bursts of openings is that these represent periods of desensitization (and that bursts of activity arise when the receptor recovers from desensitization). So, it seems safe to conclude that $\alpha7$*-nAChR can exhibit a persistent pattern of desensitization and then recovery in the extended presence of oAβ_{42}. For these reasons, we hypothesized that, in the continued presence of oAβ_{42}, the persistent activation of $\alpha7\beta2$-nAChR (exacerbated by prolonged open-dwell time induced by oAβ_{42} at this subtype) contributes to BFCN decline through alterations in BFCN intrinsic excitability. Further, these results indicate an important distinction between BFCNs from these cholinergic nuclei, demonstrating that oAβ_{42}, interacting with $\alpha7$*-nAChR, leads to enhanced BFCN intrinsic excitability within the MSDB and HDB but not within the NB. The most parsimonious explanation for the indistinguishable outcomes between MLA administration (which blocks function of all nAChR containing $\alpha7$ subunits) and nAChR $\beta2$ subunit deletion is that the oAβ_{42} effects seen in MSDB and HDB are dependent on oAβ_{42} interactions with $\alpha7\beta2$-nAChR and not homomeric $\alpha7$-nAChR. It is possible that the absence of both $\alpha4\beta2$- and $\alpha7\beta2$-nAChR oAβ_{42} can still increase the functional activity of the remaining homomeric $\alpha7$-nAChR, in turn enhancing BFCN output and thereby rescuing cognitive deficits observed in either $\beta2$-nAChR KO or APP/PS1 mice. Complementary to our findings that APP/PS1-$\beta2$ KO mice show less impairment compared with APP/PS1 mice alone, genetic deletion of the $\alpha7$-nAChR subunit in another mouse model of AD recovers learning and memory deficits associated with increased amyloid load (Dziewczapolski et al., 2009). This further supports the hypothesis that the critical $\alpha7$*-nAChR involved in mediating the deleterious effects of oAβ_{42} is the $\alpha7\beta2$-nAChR subtype.

Alterations in BFCN spike AHP contribute to enhanced BFCN firing rate and are dependent on oAβ_{42}/$\alpha7\beta2$-nAChR interactions

Next, we determined the effects of oAβ_{42}/$\alpha7\beta2$-nAChR interactions on altering the medium phase of BFCN spike mAHP, a process that contributes to regulation of neuronal firing rate and is a key determinant in regulating neuronal and network-level excitability (Santos et al., 2009; S. Chen et al., 2014; Mateos-Aparicio et al., 2014; Deng et al., 2019). Organotypic slice preparations were prepared under the same experimental conditions as noted in the preceding section. As before, these slices contained BFCNs within the MSDB (Fig. 6*A*), HDB (Fig. 6*B*), and NB (Fig. 6*C*) cholinergic nuclei. Following the 9 d incubation period, we presented a single depolarizing current pulse (500 nA; 1 s) to BFCNs in each region and measured the magnitude of the mAHP (Fig. 6*A′–C′*). In two of the regions examined, MSDB and HDB, BFCNs exposed to oAβ_{42} exhibited a significant reduction in the magnitude of the mAHP compared with scrambled oAβ_{42} controls (Fig. 6*A′-B′*). However, the effect of oAβ_{42} exposure was absent in MSDB and HDB BFCNs that were either coincubated in the presence of MLA or recorded from organotypic slices prepared from $\beta2$ nAChR KO mice. In these further controls, MSDB and HDB BFCNs showed no significant alteration in mAHP magnitude and outcomes were similar to those in the scrambled oAβ_{42} controls (Fig. 6*A′–B′*).

Conversely, BFCNs recorded from the NB exhibited no attenuation in mAHP amplitude after oAβ_{42} treatment; mAHP amplitudes were statistically indistinguishable from those of each of the control groups (Fig. 6*C′*). Together, these results demonstrate that oAβ_{42}-induced enhanced firing rate of distinct cholinergic populations (as seen in Fig. 5) may result from a reduction in BFCN mAHP magnitude. As in the preceding section, the indistinguishable outcomes between MLA and $\beta2$ nAChR KO controls suggest strongly that oAβ_{42}-induced attenuation in MSDB and HDB BFCN mAHP magnitude is dependent on the interaction between oAβ_{42} and $\alpha7\beta2$-nAChR. Furthermore, these data potentially link oAβ_{42}-$\alpha7\beta2$-nAChR interactions to functional modulation of intrinsic ionic mechanisms [e.g., small (SK) and/or large (BK) potassium channels] that are known to mediate neuronal firing rates (Bean, 2007).

oAβ_{42} exposure leads to alterations in BFCN action potential dynamics and is dependent on $\alpha7\beta2$-nAChR activation

Next, we investigated the effects of oAβ_{42} on BFCN action potential waveform by measuring the maximal rates of membrane voltage change during BFCN spike depolarization and repolarization. As in the preceding two sections, basal forebrain organotypic slices were prepared from ChAT-EGFP and $\beta2$ nAChR KO nonlittermates containing MSDB, HDB, and NB nuclei, and the same 9 d incubation protocols were applied. A ramp current injection protocol (0.1 pA/ms; 100 pA max) was used to elicit a train of action potentials from BFCNs, and phase-plane portraits were generated for MSDB, HDB, and NB BFCNs from ChAT-EGFP and $\beta2$ nAChR KO mice by plotting the maximal first-order derivative of the BFCN somatic membrane potential (dV/dt_{max}) as a function of BFNC membrane potential (Fig. 7*A–C*).

Chronic incubation in oAβ_{42} progressively and significantly reduced the dV/dt_{max} during the depolarizing phase of the spike train in MSDB (Fig. 7*A′*) and HDB BFCNs (Fig. 7*B′*). This effect of oAβ_{42} was reversed in MSDB and HDB BFCNs incubated in the presence of scrambled oAβ_{42}, those coincubated with oAβ_{42} + MLA, and was absent in those slices prepared from $\beta2$ nAChR KO mice. Notably, chronic incubation in oAβ_{42} was without effect on dV/dt_{max} during the depolarizing phase of the spike train in BFNCs located in NB (Fig. 7*C′*). The effects of oAβ_{42} were not limited to the action potential depolarization phase. Further analysis of outcomes in MSDB and HDB BFCNs revealed a progressive and significant oAβ_{42}-induced increase in the dV/dt_{max} during action potential repolarization in the spike train of MSDB (Fig. 7*A′′*) and HDB BFCNs (Fig. 7*B′′*) compared with basal forebrain organotypic slices incubated in the scrambled oAβ_{42} control. The observed oAβ_{42}-induced increase in action potential repolarization rates was also reversed by coincubation with oAβ_{42} + MLA, and absent in slices prepared from $\beta2$ nAChR KO mice, in MSDB (Fig. 7*A′′*) and HDB (Fig. 7*B′′*) BFCNs. Further, chronic incubation of NB BFCNs in oAβ_{42} did not change dV/dt_{max}

←

$p = 0.99$, Tukey's $p = 0.96$; 80 pA, oAβ_{42} = 5.5 ± 0.7 vs scrambled oAβ_{42} = 6.3 ± 0.7, $F_{(3,16)} = 1.3$, $p = 0.29$, Tukey's $p = 0.86$; 100 pA, oAβ_{42} = 7.2 ± 1.3 vs scrambled oAβ_{42} = 7.8 ± 0.9, $F_{(3,16)} = 0.47$, $p = 0.71$, Tukey's $p = 0.97$; oAβ_{42}, $n = 10$; scrambled oAβ_{42} controls, $n = 12$; oAβ_{42} + MLA, $n = 10$; $\beta2$ nAChR KO slices incubated with oAβ_{42}, $n = 10$). ***G***, Native/PAGE Western blotting to confirm soluble oAβ_{42} assemblies. Neurobasal media was collected from organotypic slice cultures immediately (time point 0; T0) and 24 h after incubation (time point 24; T24). Large molecular weight oAβ_{42} species (~680 kDa) and their intermediates (~250, 150, and 60 kDa) were present at both T0 and T24. Optical densitometry revealed no change in band intensity or shift in the relative size of soluble oAβ_{42} assemblies at T0 and T24 (right), validating that basal forebrain organotypic cultures were consistently exposed to soluble, oAβ_{42} and not insoluble protofibrillar forms of Aβ_{42}. All data analyzed using one-way ANOVA with Tukey's *post hoc* test. Data are the mean number of action potentials generated ± SEM. *$p < 0.05$. **$p < 0.01$. ***$p < 0.001$.

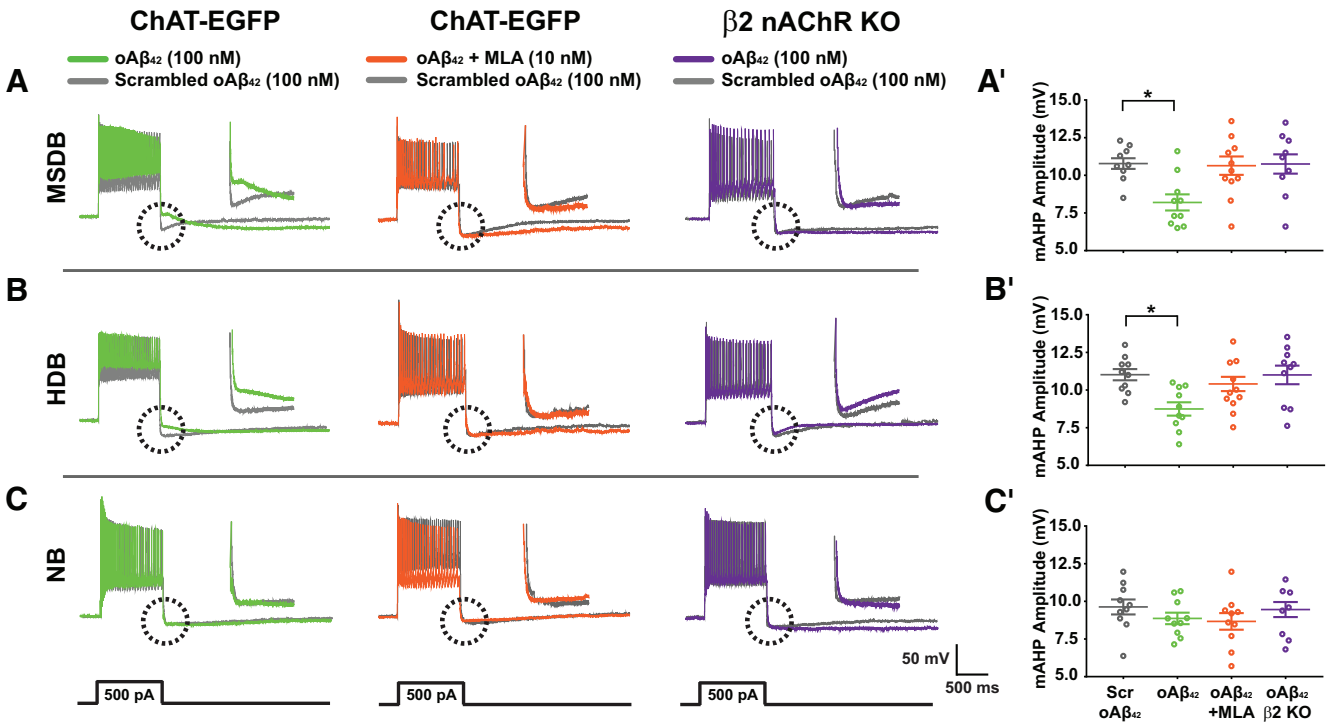

Figure 6. oAβ_{42} enhancement of BFCN intrinsic excitability results from abrogated mAHP. A single step current injection (1 s; 500 pA; shown below representative traces) was used to measure mAHP magnitude from (***A***) MSDB, (***B***) HDB, or (***C***) NB BFCNs from ChAT-EGFP organotypic slice cultures incubated with oAβ_{42} (green traces), oAβ_{42} + MLA (orange traces), or scrambled oAβ_{42} (gray traces). Organotypic slice cultures harvested from β2 nAChR subunit KO mice were incubated with oAβ_{42} (purple trace) or scrambled oAβ_{42} (gray trace). Insets, Area within dashed circle. ***A'***, MSDB BFCNs exposed to oAβ_{42} exhibited a significant reduction in the magnitude of the mAHP compared with scrambled oAβ_{42} controls (oAβ_{42}, 8.2 ± 0.5 mV, $n = 10$; scrambled oAβ_{42}, 10.8 ± 0.4 mV, $n = 9$, $F_{(3,34)} = 4.9$; $p = 0.006$, Tukey's $p = 0.022$). This effect was reversed in MSDB BFCNs incubated with oAβ_{42} in the presence of MLA or MSDB BFCNs recorded from β2 nAChR KO organotypic slice cultures incubated with oAβ_{42} (oAβ_{42} + MLA, $n = 11$, 10.6 ± 0.6 mV, Tukey's $p = 0.99$; β2 nAChR KO + oAβ_{42}, $n = 9$, 10.7 ± 0.7 mV, Tukey's $p = 0.99$). ***B'***, HDB BFCNs exhibit similar, significant, reductions in mAHP amplitude after oAβ_{42} exposure compared with scrambled oAβ_{42} controls (oAβ_{42}, 8.8 ± 0.4 mV, $n = 10$; scrambled oAβ_{42}, 11.0 ± 0.4 mV, $n = 10$, $F_{(3,36)} = 4.7$, $p = 0.007$, Tukey's $p = 0.012$). HDB BFCNs incubated with oAβ_{42} in the presence of MLA or recorded from β2 nAChR KO slices incubated with oAβ_{42} showed similar mAHP magnitude compared with scrambled oAβ_{42} controls (oAβ_{42} + MLA, 10.7 ± 0.5 mV, $n = 11$, Tukey's $p = 0.96$; β2 nAChR KO + oAβ_{42}, 10.9 ± 0.6 mV, $n = 10$, Tukey's $p = 0.99$). ***C'***, NB BFCNs showed no attenuation in mAHP amplitude after oAβ_{42} treatment and were similar to control groups (oAβ_{42}, 8.9 ± 0.4 mV, $n = 10$; scrambled oAβ_{42}, 9.6 ± 0.5 mV, $p = 0.56$, $n = 10$; MLA, 8.7 ± 0.6 mV, $p = 0.96$, $n = 10$; β2 nAChR KO + oAβ_{42}, 9.2 ± 0.6 mV, $p = 0.9$, $n = 8$; $F_{(3,34)} = 0.72$; $p = 0.54$). Symbols represent individual recordings. All data analyzed using one-way ANOVA with Tukey's *post hoc* test. Symbols represent individual recordings. Data are mean mAHP amplitude ± SEM. $*p < 0.05$.

compared with that measured in the same neurons after chronic incubation with scrambled oAβ_{42} (Fig. 7*C''*).

While no significant changes were observed in BFCN action potential threshold after oAβ_{42} administration (Fig. 7*D*), MSDB and HDB BFCNs exposed to oAβ_{42} exhibited a significant reduction in the latency to spike compared with scrambled oAβ_{42} controls (Fig. 7*E*). This effect was normalized in MSDB and HDB BFCNs coincubated in oAβ_{42} + MLA, and absent in MSDB and HDB BFCNs recordings from slices prepared from β2 nAChR KO mice and incubated with oAβ_{42} alone. Furthermore, MSDB and HDB BFCNs exposed to oAβ_{42} showed a significant reduction in action potential amplitude comparing the amplitude of the first spike generated to the last spike generated in the train of action potentials (Fig. 7*F*). Again, these changes in action potential amplitude in MSDB and HDB BFCNs were lost following coincubation of slices with oAβ_{42} + MLA, or in recordings from slices prepared from β2 nAChR KO mice incubated in oAβ_{42}. No alterations were seen in NB BFCNs incubated with oAβ_{42}, across any of these measures (action potential threshold, time to first spike, or action potential amplitude). Overall, these results demonstrate the ability of oAβ_{42} to modulate several aspects of BFCN action potential waveform, including reduced rates of spike depolarization and repolarization, latency to generate action potentials, and reduced action potential amplitude. They also demonstrate a regional specificity to oAβ_{42}-induced changes, which were consistently seen in BFCNs of the MSDB and HDB, but not those from the NB.

Genetic deletion of the β2 nAChR subunit ameliorates deficits in spatial reference memory in the APP/PS1 mouse model of AD

Expression of human APP and Aβ in transgenic mice elicits several AD-like neuropathological phenotypes that correlate strongly with aberrant neuronal activity and impairments in learning and memory (Palop et al., 2007). To determine whether nAChR that contain β2 subunits (i.e., including $\alpha7\beta$2-nAChR) mediate the cognitive deficits observed in the APP/PS1 mouse model of AD, we genetically deleted the β2 nAChR subunit gene (thus eliminating all $\alpha7\beta$2-nAChR expression within the CNS) in the APP/PS1 transgenic mouse model. We then assessed the acquisition and overnight retention of spatial reference memory using the MWM test (Fig. 8).

For both latency to platform and distance traveled, repeated-measures ANOVA revealed a main effect of Genotype (Latency: $F_{(3,28)} = 5.70$, $p = 0.006$; Distance: $F_{(3,28)} = 10.25$, $p = 0.00003$) and Day (Latency: $F_{(5,140)} = 27.27$, $p = 0.00004$; Distance: $F_{(5,140)} = 49.62$, $p = 0.00006$). A significant Genotype × Day interaction was observed for Latency (Fig. 8*A*; $F_{(15,140)} = 2.59$, $p = 0.0004$),

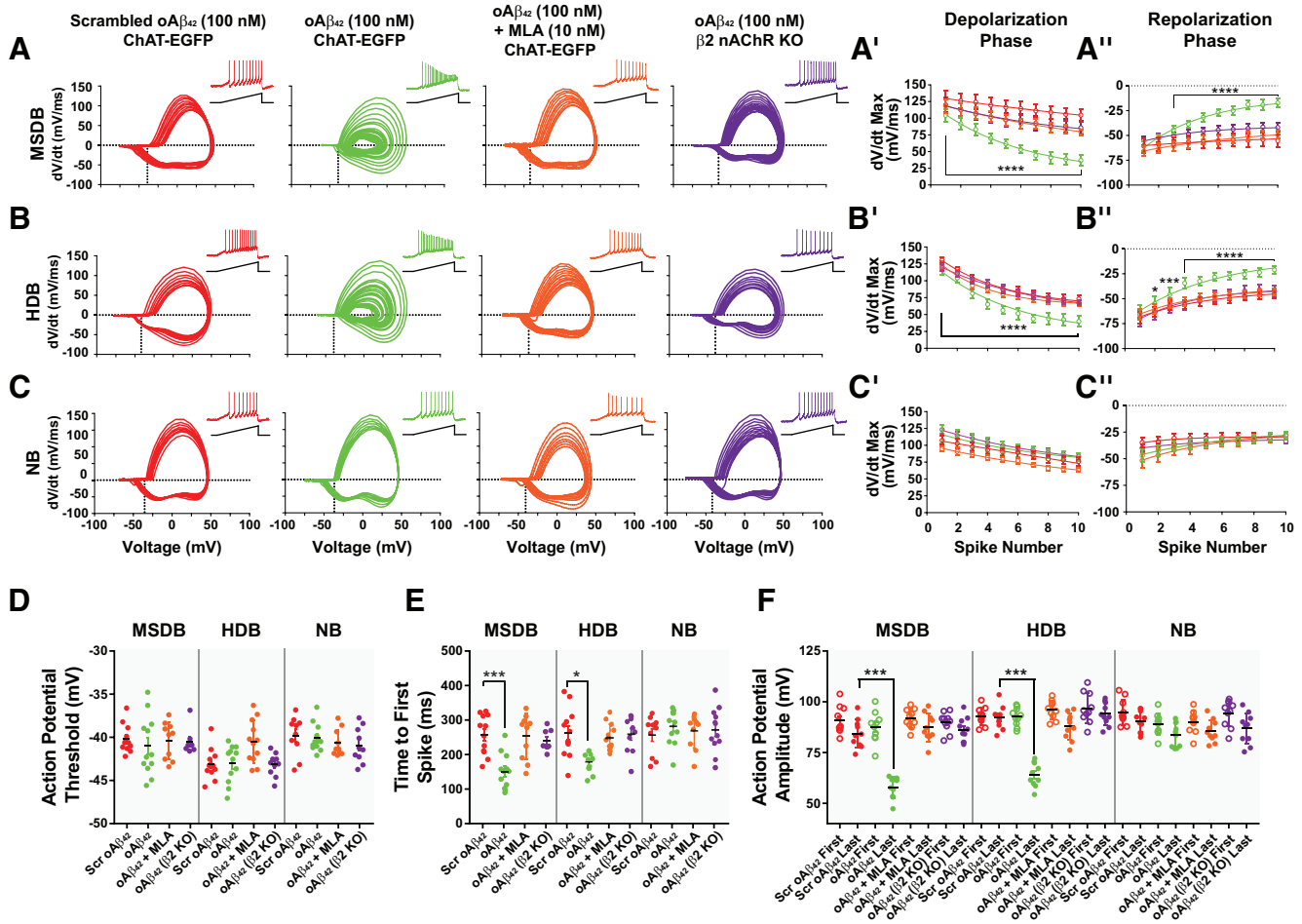

Figure 7. oAβ_{42}-induced alterations BFCN action potential dynamics. ***A–C***, Representative phase plane portraits [i.e., maximal rate of voltage change (dV/dt$_{max}$) plotted as a function of membrane potential] of BFCN action potential waveforms from MSDB, HDB, or NB BFCNs chronically incubated with scrambled oAβ_{42} (100 nM; red traces), oAβ_{42} (100 nM; green traces), or oAβ_{42} (100 nM) + MLA (50 nM; orange traces). Additional controls included MSDB, HDB, and NB BFCNs from β2 nAChR KO animals chronically incubated with oAβ_{42} (100 nM; purple traces). Insets, Action potentials generated with a ramp current injection protocol (0.1 pA/s; 100 pA max). Vertical dashed lines indicate action potential threshold. Horizontal dashed lines indicate dV/dt$_{max}$ = 0. ***A′–A′′***, Comparisons of MSDB BFCN dV/dt$_{max}$ for the first 10 spikes generated. Incubation in oAβ_{42} progressively and significantly reduced dV/dt$_{max}$ during the depolarizing phase in MSDB BFCNs compared with scrambled oAβ_{42} controls (ANOVA summary: $F_{(3,38)} = 100.2$, $p = 0.00008$; Tukey's p values: spikes 1-10 = 0.000036; oAβ_{42}, $n = 12$; scrambled oAβ_{42}, $n = 12$). Conversely, MSDB BFCNs exposed to oAβ_{42} exhibited a significant increase in dV/dt$_{max}$ during spike repolarization (ANOVA summary: $F_{(3,36)} = 39.9$, $p = 0.00003$; Tukey's p values: spike 1 = 0.98, spike 2 = 0.14, and spikes 3-10 = 0.000073; oAβ_{42}, $n = 12$; scrambled oAβ_{42}, $n = 12$). ***B′***, ***B′′***, Comparisons of HDB BFCN dV/dt$_{max}$ during spike depolarization and repolarization. HDB BFCNs exposed to oAβ_{42} exhibited a progressive and significant decrease dV/dt$_{max}$ during spike depolarization compared with scrambled oAβ_{42} controls (ANOVA summary: $F_{(3,41)} = 70.2$, $p = 0.00009$; Tukey's p values: spikes 1-10 = 0.00005; oAβ_{42}, $n = 12$; scrambled oAβ_{42}, $n = 11$) and a significant increase in dV/dt$_{max}$ during spike repolarization compared with scrambled oAβ_{42} controls (ANOVA summary: $F_{(3,41)} = 24.7$, $p = 0.00002$; Tukey's p values: spike 1 = 0.86, spike 2 = 0.03, spike 3 = 0.0002, spikes 4-10 = 0.00008; oAβ_{42}, $n = 12$; scrambled oAβ_{42}, $n = 11$). ***C′***, ***C′′***, Comparisons of NB BFCN dV/dt$_{max}$ during spike depolarization and repolarization. An effect of treatment on NB BFCN dV/dt$_{max}$ was observed [ANOVA summary (depolarization): $F_{(3,40)} = 13.5$; $p = 0.00006$; ANOVA summary (repolarization): $F_{(3,40)} = 5.4$; $p = 0.003$]. However, *post hoc* comparisons revealed no differences in dV/dt$_{max}$ between NB BFCNs exposed to oAβ_{42} versus scrambled oAβ_{42} controls during spike depolarization or repolarization [Tukey's p values (depolarization): spikes 1-10, $p = 0.85$; Tukey's p values (repolarization): spikes 1-10, $p = 0.95$; oAβ_{42}, $n = 12$; scrambled oAβ_{42}, $n = 10$]. ***D***, MSDB, HDB, and NB BFCN threshold analysis revealed no differences in spike threshold after oAβ_{42} treatment (MSDB, $F_{(3,38)} = 0.26$, $p = 0.85$, oAβ_{42}, −41.0 ± 1.0 mV vs scrambled controls −40.2 ± 0.5 mV, Tukey's $p = 0.84$; HDB, $F_{(3,42)} = 4.9$, p =0.005, oAβ_{42}, −43.0 ± 0.6 mV vs scrambled controls −43.1 ± 0.5 mV, Tukey's $p = 0.99$; NB, $F_{(3,38)} = 0.78$, $p = 0.51$, oAβ_{42}, −40.1 ± 0.5 mV vs scrambled controls −39.8 ± 0.7 mV, Tukey's $p = 0.98$). ***E***, Incubation with oAβ_{42} reduced time to first spike in MSDB ($F_{(3,38)} = 10.2$, $p = 0.00002$, oAβ_{42}, 151.0 ± 14.6 ms vs scrambled oAβ_{42}, 257.7 ± 16.5 ms; Tukey's $p = 0.0001$) and HDB BFCNs ($F_{(3,42)} = 7.1$, $p = 0.0006$, oAβ_{42}, 179.3 ± 8.6 ms, scrambled oAβ_{42}, 262.8 ± 20.4 ms; $p = 0.001$) but not NB BFCNs ($F_{(3,40)} = 0.4$, $p = 0.76$, oAβ_{42}, 282.0 ± 14.4 ms, scrambled oAβ_{42}, 256.3 ± 17.9 ms; $p = 0.99$). ***F***, oAβ_{42}-induced reduction in spike amplitude was observed in MSDB neurons ($F_{(7,72)} = 31.9$, $p = 0.00003$, oAβ_{42} last spike [closed red circles], 57.9 ± 1.6 mV, scrambled oAβ_{42} last spike [closed green circles], 84.4 ± 2.2 mV; $p = 0.0006$) and HDB neurons ($F_{(7,72)} = 35.5$, $p = 0.0008$, oAβ_{42} last spike, 64.1 ± 1.9 mV, scrambled oAβ_{42} last spike, 92.2 ± 1.8 mV; $p = 0.0003$), but not NB neurons ($F_{(7,72)} = 4.4$, $p = 0.0004$, oAβ_{42} last spike, 83.7 ± 1.8 mV, scrambled oAβ_{42} last spike, 90.4 ± 1.7 mV; $p = 0.0009$). Differences in dV/dt$_{max}$ across groups were analyzed using two-way ANOVA with Tukey's *post hoc* test. Action potential threshold, time to first spike, and action potential amplitude were analyzed using one-way ANOVA with Tukey's *post hoc* test. Data are mean mAHP amplitude ± SEM. $*p < 0.05$, $***p < 0.001$, $****p < 0.0001$.

but not Distance (Fig. 8*B*; $F_{(15,140)} = 1.53$, $p = 0.10$). *Post hoc* tests for Latency revealed that the WT group differed from the β2 nAChR KO group and the APP/PS1 group, but not the APP/PS1-β2KO group (Fig. 8*A′*; $p = 0.001$, $p = 0.0003$, and $p = 0.10$, respectively). Furthermore, the APP/PS1 group differed from APP/PS1-β2KO group (Fig. 8*A′*; $p = 0.018$). *Post hoc* tests for Distance revealed that the WT group differed from β2 nAChR KO, APP/PS1, and APP/PS1-β2KO groups (Fig. 8*B′*; p = 0.00007, $p = 0.00008$, and $p = 0.023$, respectively). The APP/PS1 group also differed from the APP/PS1-β2KO group (Fig. 8*B′*; $p = 0.033$). Together, these data suggest that, in aged mice, genetic deletion of the β2 nAChR subunit in APP/PS1 mice

Table 1. Passive membrane properties of MSDB, HDB, and NB BFCNs

	MSDB				HDB				NB			
Passive properties	Scrambled oAβ_{42}	oAβ_{42}	MLA + oAβ_{42}	β2 KO + oAβ_{42}	Scrambled oAβ_{42}	oAβ_{42}	MLA + oAβ_{42}	β2 KO + oAβ_{42}	Scrambled oAβ_{42}	oAβ_{42}	MLA + oAβ_{42}	β2 KO + oAβ_{42}
No. of neurons	$n = 13$	$n = 13$	$n = 10$	$n = 11$	$n = 12$	$n = 13$	$n = 10$	$n = 12$	$n = 15$	$n = 12$	$n = 10$	$n = 11$
Cm (pF)	52.2 ± 6.8	51.4 ± 8.4	51.8 ± 6.5	55.6 ± 12.2	55.2 ± 5.3	49.3 ± 5.4	53.6 ± 6.8	49.6 ± 10.6	57.3 ± 9.1	55.3 ± 4.3	52.7 ± 3.3	51.3 ± 7.6
Rin (mΩ)	229.3 ± 32.4	357.8 ± 47.2*	219.6 ± 27.8	241.4 ± 28.9	237.9 ± 33.6	395.2 ± 45.5*	222.3 ± 11.8	208.8 ± 25.0	186.3 ± 21.3	152.6 ± 21.1	175.6 ± 8.8	180.6 ± 38.9
RMP (mV)	−62.1 ± 3.5	−60.3 ± 3.5	−63.8 ± 4.5	−63.1 ± 4.5	−60.8 ± 5.0	−59.5 ± 4.5	−61.5 ± 6.2	−64.5 ± 4.5	−63.8 ± 6.2	−60.5 ± 3.8	−62.2 ± 3.6	−64.5 ± 4.8

Data are mean ± SEM. BFCN capacitance (C_m), input resistance (R_{in}), and RMP were analyzed using one-way ANOVA with Tukey's *post hoc* test for within-group comparisons. n = number of BFCNs for each experimental group. $*p < 0.05$.

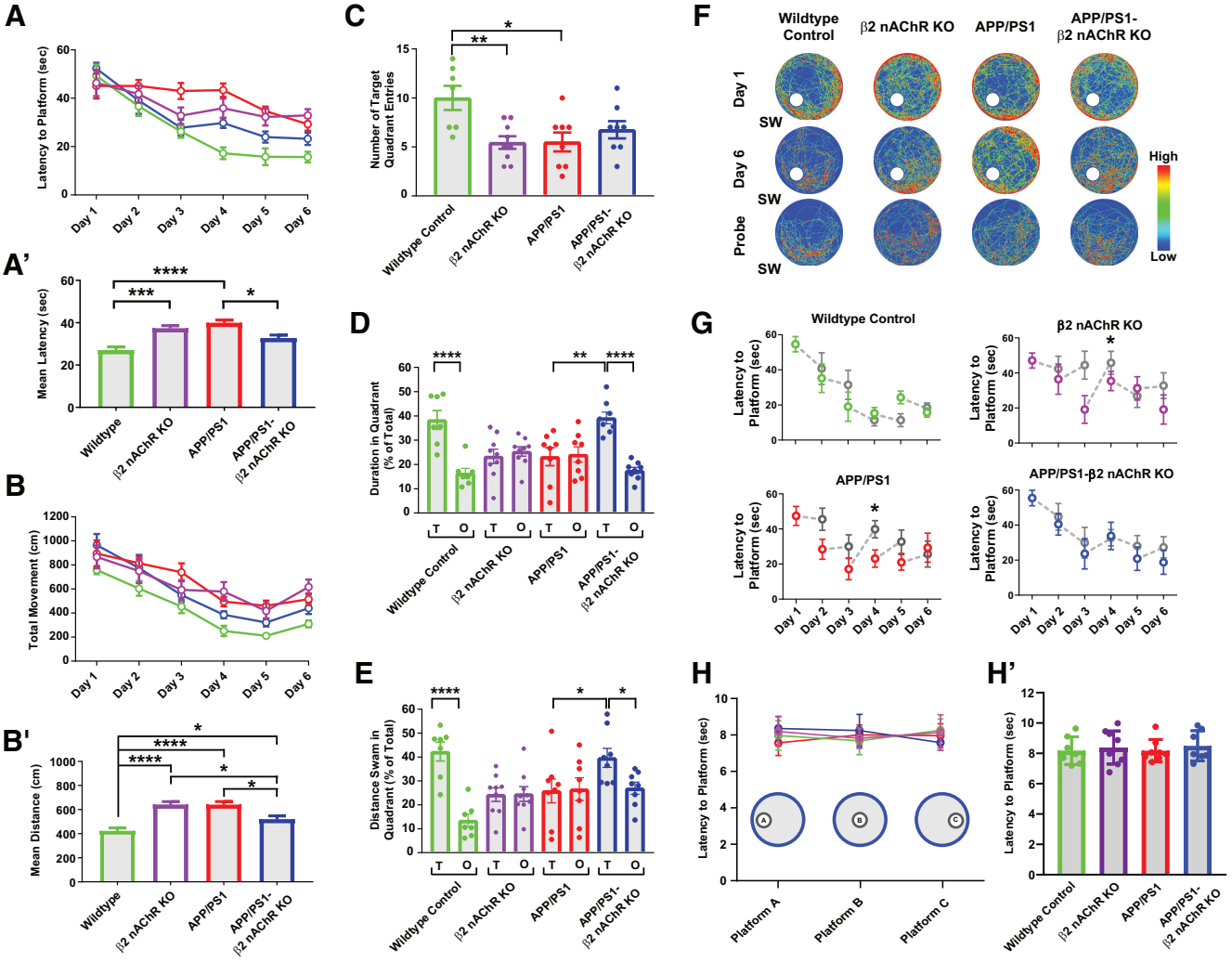

Figure 8. Genetic deletion of the β2 nAChR subunit gene alleviates spatial reference memory deficits in APP/PS1 mice. WT (green), β2 nAChR KO (purple), APP/PS1 (red), and APP/PS1-β2 KO (blue) groups were tested for spatial reference memory on days 1-6 (4 trials/day) with an additional fifth trial to test for spatial localization of the platform location. ***A***, ***A'***, Effect of genotype on latency to the platform across the first 6 d of testing and mean latency to platform collapsed across days, respectively. ***B***, ***B'***, Effect of genotype on swim distance across the first 6 d of testing and mean latency to the platform collapsed across days, respectively. ***C–E***, Probe trial data (day 6, Trial 5) measuring number of target quadrant entries, swim duration (% of total), swim distance (% of total) in target (T) or opposite (O) quadrants of the MWM. ***F***, Heat maps illustrating localization patterns in the maze on day 1 (first row), day 6 (second row), and the probe trial whereby the platform was removed (third row). ***G***, Overnight forgetting calculated between days. ***H***, ***H'***, Visual platform tests (average latency for each group at three different maze locations) conducted following spatial reference memory testing to confirm that all animals possessed the visual and motor competence to solve the swimming maze task. ***C-E***, ***H'***, Data points represent individual animals. APP/PS1-β2 nAChR KO, $N = 7$; APP/PS1, $N = 8$; β2KO, $N = 9$; WT mice, $N = 7$. Data analyzed using omnibus repeated-measures ANOVA with Fisher's LSD *post hoc* test. Student's *t* test was used for within-group comparisons. Data are mean ± SEM. $*p < 0.05$, $**p < 0.01$, $***p < 0.001$, $****p < 0.0001$.

resulted in improved learning during acquisition of the spatial reference memory task.

To test for spatial localization of the platform, a probe trial (whereby the platform was removed) was conducted on day 6 Trial 5. One-way ANOVA revealed a main effect of Genotype for target quadrant preference (Fig. 8*C*; $F_{(3,28)} = 5.01$; $p = 0.004$). *Post hoc* tests for number of target quadrant entries revealed that WT and APP/PS1-β2KO groups exhibited a greater number of target quadrant entries compared with opposite quadrant entries (Fig. 8*C*; $p = 0.00002$ and $p = 0.0004$, respectively). Target

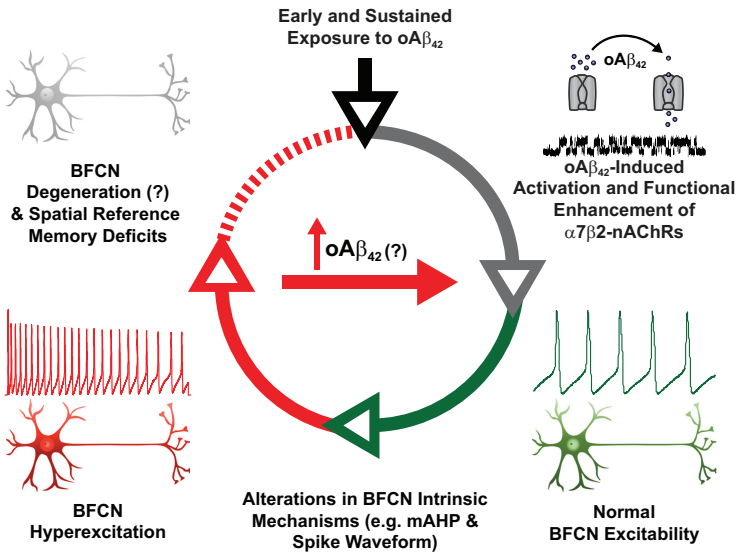

Figure 9. Working model for the role of $\alpha7\beta2$-nAChR in oAβ_{42}-induced BFCN hyperexcitation and cognitive decline. Early and sustained exposure to oAβ_{42} causes the activation and functional enhancement of $\alpha7\beta2$-nAChR (gray arrow). This leads to alterations in BFCN intrinsic mechanisms (e.g., BFCN AHP and spike waveform) possibly through the functional dysregulation of voltage and/or calcium-dependent ion channels (green arrow). As a result, these hyperexcited BFCNs may degenerate, leading to a decline in spatial reference memory processing (dotted red line). Simultaneously, BFCN hyperexcitability may lead to increased presynaptic release of oAβ_{42} (Cirrito et al., 2008), perpetuating this vicious cycle, leading to further BFCN death.

quadrant preference was absent in the APP/PS1 and the $\beta2$ nAChR KO groups ($p = 0.35$ and 0.54, respectively), indicating that these groups did not localize the platform. A main effect of Genotype was observed for swim duration in the target quadrant (Fig. 8*D*; $F_{(3,28)} = 8.88$; $p = 0.00007$). *Post hoc* test revealed that WT and APP/PS1-$\beta2$KO groups spent significantly more time in the target quadrant (T) compared with time spent in the opposite (O) quadrant (Fig. 8*D*; $p = 0.00008$ and $p = 0.00005$, respectively). APP/PS1-$\beta2$KO groups were similar to WT animals ($p = 0.99$). However, APP/PS1-$\beta2$KO mice spent significantly more time in the target quadrant than APP/PS1 mice ($p = 0.0036$). A main effect of Genotype was also observed for swim distance in the target quadrant (Fig. 8*E*; $F_{(3,28)} = 7.62$; $p = 0.0006$). *Post hoc* tests revealed that WT and APP/PS1-$\beta2$KO groups traveled further in the target quadrant (T) compared with the swim distance in the opposite (O) quadrant (Fig. 8*E*; $p = 0.00006$ and $p = 0.019$, respectively) and were indistinguishable from each other on this measure. Conversely, the $\beta2$ nAChR KO and APP/PS1 KO groups failed to localize to the target quadrant ($p = 0.94$ and 0.97, respectively). Interestingly, the APP/PS1-$\beta2$KO group swam a greater distance within the target quadrant compared with the APP/PS1 group ($p = 0.48$). These data demonstrate that the deficits in the acquisition of spatial reference memory and spatial localization of the platform location are ameliorated in APP/PS1 mice genetically null for the $\beta2$ nAChR subunit.

Next, we examined overnight forgetting by comparing Trial 4 of each day to Trial 1 of the next day, with these scores as repeated measures. A main effect of Trial (Fig. 8*G*; $F_{(3,84)} = 5.60$, $p = 0.002$) and Day ($F_{(5,140)} = 27.27$, $p = 0.00007$) was observed for Latency. A significant Trial × Day interaction was also observed for Latency ($F_{(15,420)} = 1.75$, $p = 0.013$). *Post hoc* analysis revealed that no overnight forgetting was observed in WT groups or APP/PS1-$\beta2$KO groups (Fig. 8*G*; $p = 0.76$ and $p = 0.25$, respectively). However, overnight forgetting was observed for APP/PS1 groups ($p = 0.022$) and $\beta2$ nAChR KO groups ($p = 0.021$) between days 3 and 4 of testing. These results demonstrate an important role of $\beta2$-containing nAChR in mediating day-to-day spatial reference memory retention in the APP/PS1 rodent model of AD.

Discussion

These findings demonstrate oAβ_{42}, interacting with $\alpha7\beta2$-nAChR, plays a crucial role in BFCN functional instability and may contribute to cognitive deficits commonly observed during the etiopathogenesis of AD. We show that oAβ_{42} directly activates $\alpha7$*-nAChR and preferentially enhances the open-dwell time kinetics of heteromeric $\alpha7\beta2$-nAChR. Further, oAβ_{42} interacting with both $\alpha7$- and $\alpha7\beta2$-nAChR induces neuronal hyperexcitation in specific BFCN subpopulations by increasing action potential firing rates. This effect is mediated, in MSDB and HDB BFCNs, by (1) altered action potential waveforms and (2) diminished action potential AHP. Both effects can be normalized through pharmacological antagonism or genetic deletion of $\alpha7\beta2$-nAChR. Furthermore, we demonstrate that genetic deletion of $\beta2$-nAChR subunits (and, therefore, $\alpha7\beta2$-nAChR subtypes) *in vivo* ameliorates spatial reference memory deficits in the APP/PS1 mouse AD model.

At the molecular level, studies examining $\alpha7$*-nAChR macroscopic currents provide disparate evidence regarding $\alpha7$*-nAChR activation by oAβ_{42} (Dineley et al., 2002; Fu and Jhamandas, 2003; Liu et al., 2009). Macroscopic activation of $\alpha7$*-nAChR by conventional agonists is sensitive to the timing and concentration of agonist application (Uteshev et al., 2002); this may be even more critical for oAβ_{42}. Accordingly, single-channel recordings provide a key technical advantage, as recently shown for homomeric $\alpha7$-nAChR (Lasala et al., 2019). In our present study, we show unequivocally that oAβ_{42} activates $\alpha7$- and $\alpha7\beta2$-nAChR. Here, oAβ_{42}-induced single-channel open-dwell times match those induced by ACh, with one exception. Openings of $\alpha7\beta2$-nAChRs are prolonged by oAβ_{42} compared with ACh. Our findings suggests that, while homomeric $\alpha7$-nAChR certainly may be targets for pathogenic oAβ_{42} effects (as also demonstrated by Lasala et al., 2019), the function of the narrowly distributed $\alpha7\beta2$-nAChR population may be disproportionately enhanced by oAβ_{42}. Further, oAβ_{42}'s ability to lengthen $\alpha7\beta2$-nAChR openings resembles that of a PAM (D. K. Williams et al., 2011; Andersen et al., 2016), indicating that oAβ_{42} has PAM activity at $\alpha7\beta2$-nAChR, but not $\alpha7$-nAChR. An allosteric mechanism fits with spectroscopic studies suggesting that oAβ_{42} does not occupy orthosteric binding sites (Lasala et al., 2019). It also suggests the novel possibility that introducing $\beta2$ subunits adds an allosteric oAβ_{42} binding site, perhaps at $\alpha7/\beta2$ subunit interfaces.

A wide range of oAβ_{42} concentrations is observed in AD patients (low pM to low μM range), and the effects of oAβ_{42} at 100 nM observed here fall within the neuropathologically confirmed range in AD (Yang et al., 2013, 2017). Synthetic oAβ_{42} prepared under carefully defined conditions likely replicates the forms adopted by oAβ_{42} in research animals or AD patients, and translational relevance is supported by studies using Aβ-

containing extracts from human AD subjects (Shankar et al., 2008; Puzzo et al., 2017).

In most brain regions, α7*-nAChR contain only α7 subunits. However, $\alpha7\beta2$-nAChRs are expressed in restricted neuronal populations, including BFCNs (Azam et al., 2003). Inspired by our finding that $\alpha7\beta2$-nAChRs are sensitive to functional modulation by oAβ_{42}, we examined the effects of oAβ_{42} on BFCN function. Our central novel observation was that long-term exposure to oAβ_{42} enhanced spike firing rates of MSDB and HDB BFCNs. Critically, these oAβ_{42} effects are blocked by the α7-nAChR-selective antagonist, MLA. This hyperexcitatory effect of oAβ_{42} could be viewed as a maladaptive response to sustained stimulation by oAβ_{42} of MSDB and HDB BFCNs expressing α7*-nAChR. Moreover, oAβ_{42} effects are abrogated in organotypic cultures prepared from β2-nAChR KO mice. Since the outcomes of α7*- or $\alpha7\beta2$-nAChR functional loss are indistinguishable, the most parsimonious explanation is that $\alpha7\beta2$-nAChRs are necessary and sufficient to mediate oAβ_{42}-induced hyperexcitation of MSDB and HDB BFCNs. It is possible that interactions of oAβ_{42} with both α7*- and $\alpha7\beta2$-nAChR could be important. Unfortunately, no pharmacological agents exist to isolate α7- from $\alpha7\beta2$-nAChR (Wu et al., 2016). As another example, interactions of oAβ_{42} with other β2*-nAChR may contribute to the phenomena observed. Certainly, $\alpha4\beta2$-nAChR expression seems likely on at least a subset of BFCNs, and such a nAChR population would be well placed to affect functional and behavioral outcomes.

Localized expression of $\alpha7\beta2$-nAChR on BFCNs (Liu et al., 2009; Moretti et al., 2014) may significantly contribute to these neurons' loss in early AD. Elevated oAβ_{42} may be particularly damaging to BFCNs by provoking longer-lasting openings of $\alpha7\beta2$-nAChR than does ACh. This effect may be exacerbated by oAβ_{42}'s persistence versus transient exposure to ACh, potentially prolonging otherwise self-limiting responses to ACh. Thus, BFCNs will be especially vulnerable compared with the majority of neurons expressing only homomeric α7-nAChR.

Our observations also lend insights into the active mechanisms mediating oAβ_{42}-induced enhancement of BFCN firing rates. In BFCNs from MSDB and HDB, but not from NB, we observed that oAβ_{42} (1) reduces mAHP amplitude, (2) alters the maximal rate of voltage change during BFCN spike depolarization and repolarization, and (3) reduces latency to spike generation. These processes, which contribute to the intrinsic electrical characteristics of many neurons, are shaped by the activity of specific Na^+, Ca^{2+}, and K^+ channel subtypes (Bean, 2007). Prior studies point to the role of oAβ_{42} in altering voltage- and calcium-dependent ion channels that govern neuronal excitability (Nimmrich et al., 2008; Alier et al., 2011; Gavello et al., 2018). Our findings, therefore, could reflect changes in the activity of Ca^{2+} and/or K^+ channels following sustained oAβ_{42} exposure.

In contrast, NB BFCNs are insensitive to oAβ_{42}-induced hyperexcitation. This might reflect reduced prevalence of $\alpha7\beta2$-nAChR in NB BFCNs. While PCR-based studies confirm α4-nAChR mRNA expression in MSDB BFCNs (Liu et al., 2009), ISH indicates that this is much more prominent in NB BFCNs, and in noncholinergic cells of the medial septum and mesopontine tegmentum (Azam et al., 2003). Accordingly, a greater proportion of NB β2-containing-nAChRs are likely $\alpha4\beta2$-nAChR, possibly reducing $\alpha7\beta2$-nAChR expression in this region. Furthermore, clinical studies have documented α7-nAChR subunit mRNA upregulation in NB BFCNs of human AD patients (Counts et al., 2007). This could bias the expression toward homomeric α7-nAChR. The results shown here demonstrate subregion heterogeneity of BFCN functional output with potential clinical importance.

Previous studies have shown that α7*-nAChRs are involved in hippocampal-dependent synaptic plasticity, and the hippocampus receives extensive MSDB and HDB BFCN innervation (Fabian-Fine et al., 2001; Gu et al., 2012; Changeux et al., 2015). In contrat, NB cholinergic projections primarily innervate the neocortex (mPFC), mediating top-down saliency of attention and working memory formation (Gusnard et al., 2001). Our *in vitro* studies demonstrate susceptibility of MSDB and HDB, but not NB, BFCNs to oAβ_{42}-induced neuronal instability through $\alpha7\beta2$-nAChR activation. Accordingly, we postulate that deleterious effects of elevated oAβ_{42} levels in APP/PS1 transgenic mice, working through $\alpha7\beta2$-nAChR expressed on MSDB and HDB cholinergic neurons, correlate with spatial reference memory deficits.

Importantly, other studies have shown deleterious effects of constitutive β2 KO alone on elements of memory in aged animals (Picciotto et al., 1995, 1998; Changeux et al., 1998; Zoli et al., 1999; Caldarone et al., 2000). This is compatible with our own observations of cognitive deficits in β2 KO mice relative to WT controls. While we believe that $\alpha7\beta2$-nAChRs are key mediators of the cognitive deficits observed in APP/PS1 mice, the poor performance of β2-nAChR KO mice during MWM testing may be because of the absence of $\alpha4\beta2$-nAChR. Indeed, α7*-nAChR activity enhances LTP and memory in rodent models (Puzzo et al., 2008) and physiological roles for Aβ-induced memory enhancement have been proposed (Morley et al., 2010). Our novel finding is that deficits in spatial memory, which are observed in β2-nAChR KO as well as APP/PS1 mice, are neutralized in APP/PS1-β2 KO mice. One possible explanation is, in the absence of both $\alpha4\beta2$- and $\alpha7\beta2$-nAChR, oAβ_{42} can still increase the functional activity of the remaining homomeric α7-nAChR, in turn enhancing BFCN output and thereby rescuing cognitive deficits observed in either β2-nAChR KO or APP/PS1 mice. Complementary to our findings that APP/PS1-β2 KO mice show less impairment compared with APP/PS1 mice alone, genetic deletion of the α7 nAChR subunit in another mouse model of AD recovers learning and memory deficits associated with increased amyloid load (Dziewczapolski et al., 2009). This further supports the hypothesis that the critical α7*-nAChR involved in mediating the deleterious effects of oAβ_{42} is the $\alpha7\beta2$-nAChR subtype.

Our results clearly link $\alpha7\beta2$-nAChR to BFCN hyperexcitation, expanding on prior findings that Aβ exposure increases neuronal activity (Palop et al., 2007; Busche et al., 2008) and that persistent neuronal excitability elevates Aβ levels (Bero et al., 2011). Thus, we provide a working model (Fig. 9) describing early elevations in oAβ_{42} leading to activation of α7*-nAChR and persistent $\alpha7\beta2$-nAChR functional enhancement. Enhanced $\alpha7\beta2$-nAChR signaling alters the function of BFCN intrinsic ionic mechanisms (e.g., Ca^{2+} and/or K^+ channels) mediating BFCN excitability, producing BFCN hyperexcitation. These mechanisms, coupled with increased levels of oAβ_{42} possibly because of activity-dependent synaptic release (Cirrito et al., 2008), may induce a destabilizing feedback loop further elevating oAβ_{42} levels and, in turn, lead to BFCN degeneration and memory decline. Bringing further potential translational relevance, such hyperexcitation may also contribute to observations that seizures and subclinical epileptiform activity are increased in early AD (Vossel et al., 2013), together with hyperexcitability in neuronal circuits (O'Brien et al., 2010; Petrache et al., 2019).

References

Alier K, Ma L, Yang J, Westaway D, Jhamandas JH (2011) Abeta inhibition of ionic conductance in mouse basal forebrain neurons is dependent upon the cellular prion protein PrPC. J Neurosci 31:16292–16297.

Andersen ND, Corradi J, Sine SM, Bouzat C (2013) Stoichiometry for activation of neuronal alpha7 nicotinic receptors. Proc Natl Acad Sci USA 110:20819–20824.

Andersen ND, Nielsen BE, Corradi J, Tolosa MF, Feuerbach D, Arias HR, Bouzat C (2016) Exploring the positive allosteric modulation of human alpha7 nicotinic receptors from a single-channel perspective. Neuropharmacology 107:189–200.

Azam L, Winzer-Serhan U, Leslie FM (2003) Co-expression of alpha7 and beta2 nicotinic acetylcholine receptor subunit mRNAs within rat brain cholinergic neurons. Neuroscience 119:965–977.

Bean BP (2007) The action potential in mammalian central neurons. Nat Rev Neurosci 8:451–465.

Bero AW, Yan P, Roh JH, Cirrito JR, Stewart FR, Raichle ME, Lee JM, Holtzman DM (2011) Neuronal activity regulates the regional vulnerability to amyloid-beta deposition. Nat Neurosci 14:750–756.

Bimonte-Nelson HA, Daniel JM, Koebele SV (2015) The maze book: theories, practice, and protocols for testing rodent cognition, pp 37–72. New York: Springer.

Bouzat C, Sine SM (2018) Nicotinic acetylcholine receptors at the single-channel level. Br J Pharmacol 175:1789–1804.

Braden BB, Talboom JS, Crain ID, Simard AR, Lukas RJ, Prokai L, Scheldrup MR, Bowman BL, Bimonte-Nelson HA (2010) Medroxyprogesterone acetate impairs memory and alters the GABAergic system in aged surgically menopausal rats. Neurobiol Learn Mem 93:444–453.

Buendia I, Parada E, Navarro E, Leon R, Negredo P, Egea J, Lopez MG (2016) Subthreshold concentrations of melatonin and galantamine improve pathological AD: hallmarks in hippocampal organotypic cultures. Mol Neurobiol 53:3338–3348.

Busche MA, Eichhoff G, Adelsberger H, Abramowski D, Wiederhold KH, Haass C, Staufenbiel M, Konnerth A, Garaschuk O (2008) Clusters of hyperactive neurons near amyloid plaques in a mouse model of Alzheimer's disease. Science 321:1686–1689.

Busche MA, Chen X, Henning HA, Reichwald J, Staufenbiel M, Sakmann B, Konnerth A (2012) Critical role of soluble amyloid-beta for early hippocampal hyperactivity in a mouse model of Alzheimer's disease. Proc Natl Acad Sci USA 109:8740–8745.

Caccamo A, Ferreira E, Branca C, Oddo S (2017) p62 improves AD-like pathology by increasing autophagy. Mol Psychiatry 22:865–873.

Caldarone BJ, Duman CH, Picciotto MR (2000) Fear conditioning and latent inhibition in mice lacking the high affinity subclass of nicotinic acetylcholine receptors in the brain. Neuropharmacology 39:2779–2784.

Changeux JP, Bertrand D, Corringer PJ, Dehaene S, Edelstein S, Lena C, Le Novere N, Marubio L, Picciotto M, Zoli M (1998) Brain nicotinic receptors: structure and regulation, role in learning and reinforcement. Brain Res Brain Res Rev 26:198–216.

Changeux JP, Corringer PJ, Maskos U (2015) The nicotinic acetylcholine receptor: from molecular biology to cognition. Neuropharmacology 96:135–136.

Chen S, Benninger F, Yaari Y (2014) Role of small conductance Ca(2)(+)-activated K(+) channels in controlling CA1 pyramidal cell excitability. J Neurosci 34:8219–8230.

Chen XQ, Mobley WC (2019) Exploring the pathogenesis of Alzheimer disease in basal forebrain cholinergic neurons: converging insights from alternative hypotheses. Front Neurosci 13:446.

Cirrito JR, Kang JE, Lee J, Stewart FR, Verges DK, Silverio LM, Bu G, Mennerick S, Holtzman DM (2008) Endocytosis is required for synaptic activity-dependent release of amyloid-beta in vivo. Neuron 58:42–51.

Colquhoun D, Sakmann B (1985) Fast events in single-channel currents activated by acetylcholine and its analogues at the frog muscle end-plate. J Physiol 369:501–557.

Corradi J, Bouzat C (2016) Understanding the bases of function and modulation of alpha7 nicotinic receptors: implications for drug discovery. Mol Pharmacol 90:288–299.

Counts SE, He B, Che S, Ikonomovic MD, DeKosky ST, Ginsberg SD, Mufson EJ (2007) Alpha7 nicotinic receptor up-regulation in cholinergic basal forebrain neurons in Alzheimer disease. Arch Neurol 64:1771–1776.

Dao DQ, Perez EE, Teng Y, Dani JA, De Biasi M (2014) Nicotine enhances excitability of medial habenular neurons via facilitation of neurokinin signaling. J Neurosci 34:4273–4284.

Deng PY, Carlin D, Oh YM, Myrick LK, Warren ST, Cavalli V, Klyachko VA (2019) Voltage-independent SK-channel dysfunction causes neuronal hyperexcitability in the hippocampus of Fmr1 knock-out mice. J Neurosci 39:28–43.

Dineley KT, Xia X, Bui D, Sweatt JD, Zheng H (2002) Accelerated plaque accumulation, associative learning deficits, and up-regulation of alpha 7 nicotinic receptor protein in transgenic mice co-expressing mutant human presenilin 1 and amyloid precursor proteins. J Biol Chem 277:22768–22780.

Dziewczapolski G, Glogowski CM, Masliah E, Heinemann SF (2009) Deletion of the alpha 7 nicotinic acetylcholine receptor gene improves cognitive deficits and synaptic pathology in a mouse model of Alzheimer's disease. J Neurosci 29:8805–8815.

Eaton JB, Peng JH, Schroeder KM, George AA, Fryer JD, Krishnan C, Buhlman L, Kuo YP, Steinlein O, Lukas RJ (2003) Characterization of human alpha 4 beta 2-nicotinic acetylcholine receptors stably and heterologously expressed in native nicotinic receptor-null SH-EP1 human epithelial cells. Mol Pharmacol 64:1283–1294.

Eaton JB, Lucero LM, Stratton H, Chang Y, Cooper JF, Lindstrom JM, Lukas RJ, Whiteaker P (2014) The unique alpha4$^{+/-}$alpha4 agonist binding site in (alpha4)3(beta2)2 subtype nicotinic acetylcholine receptors permits differential agonist desensitization pharmacology versus the (alpha4)2(beta2)3 subtype. J Pharmacol Exp Ther 348:46–58.

Fá M, Puzzo D, Piacentini R, Staniszewski A, Zhang H, Baltrons MA, Li Puma DD, Chatterjee I, Li J, Saeed F, Berman HL, Ripoli C, Gulisano W, Gonzalez J, Tian H, Costa JA, Lopez P, Davidowitz E, Yu WH, Haroutunian V, et al. (2016) Extracellular tau oligomers produce an immediate impairment of LTP and memory. Sci Rep 6:19393.

Fabian-Fine R, Skehel P, Errington ML, Davies HA, Sher E, Stewart MG, Fine A (2001) Ultrastructural distribution of the alpha7 nicotinic acetylcholine receptor subunit in rat hippocampus. J Neurosci 21:7993–8003.

Fryer JD, Lukas RJ (1999) Antidepressants noncompetitively inhibit nicotinic acetylcholine receptor function. J Neurochem 72:1117–1124.

Fu W, Jhamandas JH (2003) Beta-amyloid peptide activates non-alpha7 nicotinic acetylcholine receptors in rat basal forebrain neurons. J Neurophysiol 90:3130–3136.

Gavello D, Calorio C, Franchino C, Cesano F, Carabelli V, Carbone E, Marcantoni A (2018) Early alterations of hippocampal neuronal firing induced by Abeta42. Cereb Cortex 28:433–446.

George AA, Bloy A, Miwa JM, Lindstrom JM, Lukas RJ, Whiteaker P (2017) Isoform-specific mechanisms of alpha3beta4*-nicotinic acetylcholine receptor modulation by the prototoxin lynx1. FASEB J 31:1398–1420.

Grothe M, Heinsen H, Teipel SJ (2012) Atrophy of the cholinergic basal forebrain over the adult age range and in early stages of Alzheimer's disease. Biol Psychiatry 71:805–813.

Grothe MJ, Ewers M, Krause B, Heinsen H, Teipel SJ, Alzheimer's Disease Neuroimaging Initiative (2014) Basal forebrain atrophy and cortical amyloid deposition in nondemented elderly subjects. Alzheimers Dement 10:S344–S353.

Gu S, Matta JA, Lord B, Harrington AW, Sutton SW, Davini WB, Bredt DS (2016) Brain alpha7 nicotinic acetylcholine receptor assembly requires NACHO. Neuron 89:948–955.

Gu Z, Lamb PW, Yakel JL (2012) Cholinergic coordination of presynaptic and postsynaptic activity induces timing-dependent hippocampal synaptic plasticity. J Neurosci 32:12337–12348.

Gulisano W, Melone M, Ripoli C, Tropea MR, Li Puma DD, Giunta S, Cocco S, Marcotulli D, Origlia N, Palmeri A, Arancio O, Conti F, Grassi C, Puzzo D (2019) Neuromodulatory action of picomolar extracellular Abeta42 oligomers on presynaptic and postsynaptic mechanisms underlying synaptic function and memory. J Neurosci 39:5986–6000.

Gusnard DA, Akbudak E, Shulman GL, Raichle ME (2001) Medial prefrontal cortex and self-referential mental activity: relation to a default mode of brain function. Proc Natl Acad Sci USA 98:4259–4264.

Hampel H, Mesulam MM, Cuello AC, Khachaturian AS, Vergallo A, Farlow MR, Snyder PJ, Giacobini E, Khachaturian ZS (2019) Revisiting the cholinergic hypothesis in Alzheimer's disease: emerging evidence from translational and clinical research. J Prev Alzheimers Dis 6:2–15.

Hedrick T, Danskin B, Larsen RS, Ollerenshaw D, Groblewski P, Valley M, Olsen S, Waters J (2016) Characterization of channelrhodopsin and

archaerhodopsin in cholinergic neurons of Cre-Lox transgenic mice. PLoS One 11:e0156596.

Hey JA, Yu JY, Versavel M, Abushakra S, Kocis P, Power A, Kaplan PL, Amedio J, Tolar M (2018) Clinical pharmacokinetics and safety of ALZ-801, a novel prodrug of tramiprosate in development for the treatment of Alzheimer's disease. Clin Pharmacokinet 57:315–333.

Jack CR, Bennett DA, Blennow K, Carrillo MC, Dunn B, Haeberlein SB, Holtzman DM, Jagust W, Jessen F, Karlawish J, Liu E, Molinuevo JL, Montine T, Phelps C, Rankin KP, Rowe CC, Scheltens P, Siemers E, Snyder HM, Sperling R Jr (2018) NIA-AA research framework: toward a biological definition of Alzheimer's disease. Alzheimers Dement 14:535–562.

Jongbloed W, Bruggink KA, Kester MI, Visser PJ, Scheltens P, Blankenstein MA, Verbeek MM, Teunissen CE, Veerhuis R (2015) Amyloid-beta oligomers relate to cognitive decline in Alzheimer's disease. J Alzheimers Dis 45:35–43.

Kawai H, Zago W, Berg DK (2002) Nicotinic alpha 7 receptor clusters on hippocampal GABAergic neurons: regulation by synaptic activity and neurotrophins. J Neurosci 22:7903–7912.

Khiroug SS, Harkness PC, Lamb PW, Sudweeks SN, Khiroug L, Millar NS, Yakel JL (2002) Rat nicotinic ACh receptor alpha7 and beta2 subunits co-assemble to form functional heteromeric nicotinic receptor channels. J Physiol 540:425–434.

Koebele SV, Palmer JM, Hadder B, Melikian R, Fox C, Strouse IM, DeNardo DF, George C, Daunis E, Nimer A, Mayer LP, Dyer CA, Bimonte-Nelson HA (2019) Hysterectomy uniquely impacts spatial memory in a rat model: a role for the nonpregnant uterus in cognitive processes. Endocrinology 160:1–19.

Koppensteiner P, Trinchese F, Fá M, Puzzo D, Gulisano W, Yan S, Poussin A, Liu S, Orozco I, Dale E, Teich AF, Palmeri A, Ninan I, Boehm S, Arancio O (2016) Time-dependent reversal of synaptic plasticity induced by physiological concentrations of oligomeric Abeta42: an early index of Alzheimer's disease. Sci Rep 6:32553.

Lasala M, Fabiani C, Corradi J, Antollini S, Bouzat C (2019) Molecular modulation of human alpha7 nicotinic receptor by amyloid-beta peptides. Front Cell Neurosci 13:37.

Liu Q, Huang Y, Xue F, Simard A, DeChon J, Li G, Zhang J, Lucero L, Wang M, Sierks M, Hu G, Chang Y, Lukas RJ, Wu J (2009) A novel nicotinic acetylcholine receptor subtype in basal forebrain cholinergic neurons with high sensitivity to amyloid peptides. J Neurosci 29:918–929.

Liu Q, Huang Y, Shen J, Steffensen S, Wu J (2012) Functional alpha7beta2 nicotinic acetylcholine receptors expressed in hippocampal interneurons exhibit high sensitivity to pathological level of amyloid beta peptides. BMC Neurosci 13:155.

Liu Q, Xie X, Lukas RJ, St John PA, Wu J (2013) A novel nicotinic mechanism underlies beta-amyloid-induced neuronal hyperexcitation. J Neurosci 33:7253–7263.

Lukas RJ (1993) Expression of ganglia-type nicotinic acetylcholine receptors and nicotinic ligand binding sites by cells of the IMR-32 human neuroblastoma clonal line. J Pharmacol Exp Ther 265:294–302.

Mateos-Aparicio P, Murphy R, Storm JF (2014) Complementary functions of SK and Kv7/M potassium channels in excitability control and synaptic integration in rat hippocampal dentate granule cells. J Physiol 592:669–693.

Matta JA, Gu S, Davini WB, Lord B, Siuda ER, Harrington AW, Bredt DS (2017) NACHO mediates nicotinic acetylcholine receptor function throughout the brain. Cell Rep 19:688–696.

McKenna JT, Yang C, Franciosi S, Winston S, Abarr KK, Rigby MS, Yanagawa Y, McCarley RW, Brown RE (2013) Distribution and intrinsic membrane properties of basal forebrain GABAergic and parvalbumin neurons in the mouse. J Comp Neurol 521:1225–1250.

Mesulam MM (2013) Cholinergic circuitry of the human nucleus basalis and its fate in Alzheimer's disease. J Comp Neurol 521:4124–4144.

Minkeviciene R, Rheims S, Dobszay MB, Zilberter M, Hartikainen J, Fulop L, Penke B, Zilberter Y, Harkany T, Pitkanen A, Tanila H (2009) Amyloid beta-induced neuronal hyperexcitability triggers progressive epilepsy. J Neurosci 29:3453–3462.

Moretti M, Zoli M, George AA, Lukas RJ, Pistillo F, Maskos U, Whiteaker P, Gotti C (2014) The novel alpha7beta2-nicotinic acetylcholine receptor subtype is expressed in mouse and human basal forebrain: biochemical and pharmacological characterization. Mol Pharmacol 86:306–317.

Morley JE, Farr SA, Banks WA, Johnson SN, Yamada KA, Xu L (2010) A physiological role for amyloid-beta protein: enhancement of learning and memory. J Alzheimers Dis 19:441–449.

Murray TA, Bertrand D, Papke RL, George AA, Pantoja R, Srinivasan R, Liu Q, Wu J, Whiteaker P, Lester HA, Lukas RJ (2012) $\alpha7\beta2$ nicotinic acetylcholine receptors assemble, function, and are activated primarily via their $\alpha7$-$\alpha7$ interfaces. Mol Pharmacol 81:175–188.

Nashmi R, Dickinson ME, McKinney S, Jareb M, Labarca C, Fraser SE, Lester HA (2003) Assembly of alpha4beta2 nicotinic acetylcholine receptors assessed with functional fluorescently labeled subunits: effects of localization, trafficking, and nicotine-induced upregulation in clonal mammalian cells and in cultured midbrain neurons. J Neurosci 23:11554–11567.

Neher E (1992) Correction for liquid junction potentials in patch-clamp experiments. Methods Enzymol 207:123–131.

Nicoll JA, Buckland GR, Harrison CH, Page A, Harris S, Love S, Neal JW, Holmes C, Boche D (2019) Persistent neuropathological effects 14 years following amyloid-beta immunization in Alzheimer's disease. Brain 142:2113–2126.

Nielsen BE, Minguez T, Bermudez I, Bouzat C (2018) Molecular function of the novel alpha7beta2 nicotinic receptor. Cell Mol Life Sci 75:2457–2471.

Nimmrich V, Ebert U (2009) Is Alzheimer's disease a result of presynaptic failure? Synaptic dysfunctions induced by oligomeric beta-amyloid. Rev Neurosci 20:1–12.

Nimmrich V, Grimm C, Draguhn A, Barghorn S, Lehmann A, Schoemaker H, Hillen H, Gross G, Ebert U, Bruehl C (2008) Amyloid beta oligomers (A beta(1-42) globulomer) suppress spontaneous synaptic activity by inhibition of P/Q-type calcium currents. J Neurosci 28:788–797.

O'Brien JL, O'Keefe KM, LaViolette PS, DeLuca AN, Blacker D, Dickerson BC, Sperling RA (2010) Longitudinal fMRI in elderly reveals loss of hippocampal activation with clinical decline. Neurology 74:1969–1976.

Palop JJ, Mucke L (2009) Epilepsy and cognitive impairments in Alzheimer disease. Arch Neurol 66:435–440.

Palop JJ, Chin J, Roberson ED, Wang J, Thwin MT, Bien-Ly N, Yoo J, Ho KO, Yu GQ, Kreitzer A, Finkbeiner S, Noebels JL, Mucke L (2007) Aberrant excitatory neuronal activity and compensatory remodeling of inhibitory hippocampal circuits in mouse models of Alzheimer's disease. Neuron 55:697–711.

Panza F, Lozupone M, Logroscino G, Imbimbo BP (2019) A critical appraisal of amyloid-beta-targeting therapies for Alzheimer disease. Nat Rev Neurol 15:73–88.

Papke RL, Oswald RE (1989) Mechanisms of noncompetitive inhibition of acetylcholine-induced single-channel currents. J Gen Physiol 93:785–811.

Pereira C, Agostinho P, Moreira PI, Cardoso SM, Oliveira CR (2005) Alzheimer's disease-associated neurotoxic mechanisms and neuroprotective strategies. Curr Drug Targets CNS Neurol Disord 4:383–403.

Petrache AL, Rajulawalla A, Shi A, Wetzel A, Saito T, Saido TC, Harvey K, Ali AB (2019) Aberrant excitatory-inhibitory synaptic mechanisms in entorhinal cortex microcircuits during the pathogenesis of Alzheimer's disease. Cereb Cortex 29:1834–1850.

Picciotto MR, Zoli M, Lena C, Bessis A, Lallemand Y, Le Novere N, Vincent P, Pich EM, Brulet P, Changeux JP (1995) Abnormal avoidance learning in mice lacking functional high-affinity nicotine receptor in the brain. Nature 374:65–67.

Picciotto MR, Zoli M, Rimondini R, Lena C, Marubio LM, Pich EM, Fuxe K, Changeux JP (1998) Acetylcholine receptors containing the beta2 subunit are involved in the reinforcing properties of nicotine. Nature 391:173–177.

Picciotto MR, Higley MJ, Mineur YS (2012) Acetylcholine as a neuromodulator: cholinergic signaling shapes nervous system function and behavior. Neuron 76:116–129.

Puzzo D, Privitera L, Leznik E, Fá M, Staniszewski A, Palmeri A, Arancio O (2008) Picomolar amyloid-beta positively modulates synaptic plasticity and memory in hippocampus. J Neurosci 28:14537–14545.

Puzzo D, Piacentini R, Fá M, Gulisano W, Li Puma DD, Staniszewski A, Zhang H, Tropea MR, Cocco S, Palmeri A, Fraser P, D'Adamio L, Grassi C, Arancio O (2017) LTP and memory impairment caused by extracellular Abeta and Tau oligomers is APP-dependent. Elife 6:e26991.

Santos SF, Pierrot N, Morel N, Gailly P, Sindic C, Octave JN (2009) Expression of human amyloid precursor protein in rat cortical neurons inhibits calcium oscillations. J Neurosci 29:4708–4718.

Scheltens P, Blennow K, Breteler MM, de Strooper B, Frisoni GB, Salloway S, Van der Flier WM (2016) Alzheimer's disease. Lancet 388:505–517.

Schmitz TW, Nathan Spreng R, Alzheimer's Disease Neuroimaging Initiative (2016) Basal forebrain degeneration precedes and predicts the cortical spread of Alzheimer's pathology. Nat Commun 7:13249.

Selkoe DJ (2002) Alzheimer's disease is a synaptic failure. Science 298:789–791.

Shankar GM, Li S, Mehta TH, Garcia-Munoz A, Shepardson NE, Smith I, Brett FM, Farrell MA, Rowan MJ, Lemere CA, Regan CM, Walsh DM, Sabatini BL, Selkoe DJ (2008) Amyloid-beta protein dimers isolated directly from Alzheimer's brains impair synaptic plasticity and memory. Nat Med 14:837–842.

Stine WB, Jungbauer L, Yu C, LaDu MJ (2011) Preparing synthetic Abeta in different aggregation states. Methods Mol Biol 670:13–32.

Stoppini L, Buchs PA, Muller D (1991) A simple method for organotypic cultures of nervous tissue. J Neurosci Methods 37:173–182.

Thinschmidt JS, Frazier CJ, King MA, Meyer EM, Papke RL (2005) Medial septal/diagonal band cells express multiple functional nicotinic receptor subtypes that are correlated with firing frequency. Neurosci Lett 389:163–168.

Ting JT, Daigle TL, Chen Q, Feng G (2014) Acute brain slice methods for adult and aging animals: application of targeted patch-clamp analysis and optogenetics. Methods Mol Biol 1183:221–242.

Unal CT, Golowasch JP, Zaborszky L (2012) Adult mouse basal forebrain harbors two distinct cholinergic populations defined by their electrophysiology. Front Behav Neurosci 6:21.

Uteshev VV, Meyer EM, Papke RL (2002) Activation and inhibition of native neuronal alpha-bungarotoxin-sensitive nicotinic ACh receptors. Brain Res 948:33–46.

van Goethem NP, Paes D, Puzzo D, Fedele E, Rebosio C, Gulisano W, Palmeri A, Wennogle LP, Peng Y, Bertrand D, Prickaerts J (2019) Antagonizing alpha7 nicotinic receptors with methyllycaconitine (MLA) potentiates receptor activity and memory acquisition. Cell Signal 62:109338.

Vossel KA, Tartaglia MC, Nygaard HB, Zeman AZ, Miller BL (2017) Epileptic activity in Alzheimer's disease: causes and clinical relevance. Lancet Neurol 16:311–322.

Vossel KA, Beagle AJ, Rabinovici GD, Shu H, Lee SE, Naasan G, Hegde M, Cornes SB, Henry ML, Nelson AB, Seeley WW, Geschwind MD, Gorno-Tempini ML, Shih T, Kirsch HE, Garcia PA, Miller BL, Mucke L (2013) Seizures and epileptiform activity in the early stages of Alzheimer disease. JAMA Neurol 70:1158–1166.

Walsh DM, Klyubin I, Fadeeva JV, Cullen WK, Anwyl R, Wolfe MS, Rowan MJ, Selkoe DJ (2002) Naturally secreted oligomers of amyloid beta protein potently inhibit hippocampal long-term potentiation in vivo. Nature 416:535–539.

Weltzin MM, George AA, Lukas RJ, Whiteaker P (2019) Distinctive single-channel properties of alpha4beta2-nicotinic acetylcholine receptor isoforms. PLoS One 14:e0213143.

Williams DK, Wang J, Papke RL (2011) Investigation of the molecular mechanism of the alpha7 nicotinic acetylcholine receptor positive allosteric modulator PNU-120596 provides evidence for two distinct desensitized states. Mol Pharmacol 80:1013–1032.

Williams MT, Morford LL, Wood SL, Wallace TL, Fukumura M, Broening HW, Vorhees CV (2003) Developmental D-methamphetamine treatment selectively induces spatial navigation impairments in reference memory in the Morris water maze while sparing working memory. Synapse 48:138–148.

Wu J, Liu Q, Tang P, Mikkelsen JD, Shen J, Whiteaker P, Yakel JL (2016) Heteromeric alpha7beta2 nicotinic acetylcholine receptors in the brain. Trends Pharmacol Sci 37:562–574.

Yang T, Hong S, O'Malley T, Sperling RA, Walsh DM, Selkoe DJ (2013) New ELISAs with high specificity for soluble oligomers of amyloid beta-protein detect natural Abeta oligomers in human brain but not CSF. Alzheimers Dement 9:99–112.

Yang T, Li S, Xu H, Walsh DM, Selkoe DJ (2017) Large soluble oligomers of amyloid beta-protein from Alzheimer brain are far less neuroactive than the smaller oligomers to which they dissociate. J Neurosci 37:152–163.

Yu Y, Shu Y, McCormick DA (2008) Cortical action potential backpropagation explains spike threshold variability and rapid-onset kinetics. J Neurosci 28:7260–7272.

Zaborszky L, Van den Pol AN, Gyengesi E (2012) The basal forebrain cholinergic projection system in mice. In: The mouse nervous system (Watson C, Paxinos G, Puelles L, eds), pp 684–718.

Zoli M, Picciotto MR, Ferrari R, Cocchi D, Changeux JP (1999) Increased neurodegeneration during ageing in mice lacking high-affinity nicotine receptors. EMBO J 18:1235–1244.